This is to certify that the

thesis entitled
Velocity Field Measurement for a
Uni-Directional Solidification of an
Ammonium Chloride ($NH_4Cl$) Solution
using Molecular Tagging Velocimetry (MTV)

presented by

CHEE LEONG LUM

has been accepted towards fulfillment
of the requirements for

Masters of Science degree in Mechanical Engineering

M.M. Koochesfahani

Major professor
Dr. M.M. Koochesfahani

Date July 31, 2001

# VELOCITY FIELD MEASUREMENT FOR A UNI-DIRECTIONAL SOLIDIFICATION OF AN AMMONIUM CHLORIDE ($NH_4CL$) SOLUTION USING MOLECULAR TAGGING VELOCIMETRY (MTV)

By

Chee Leong Lum

AN ABSTRACT OF A THESIS

Submitted to
Michigan State University
in partial fulfillment of the requirements
for the degree of

MASTER OF SCIENCE

Department of Mechanical Engineering

2001

Dr. Manoochehr M. Koochesfahani

ABSTRACT

THE VELOCITY FIELD MEASUREMENT IN A UNI-DIRECTIONAL SOLIDIFICATION OF AMMONIUM CHLORIDE ($NH_4Cl$) USING MOLECULAR TAGGING VELOCIMETRY (MTV)

By

Chee Leong Lum

During the solidification of a binary alloy under off-eutectic conditions, solutal and thermal forces can produce imperfections in the form of solute-rich channels. Many researchers observe that the use of uni-directional solidification for alloys can provide increased resistance to creep and thermal fatigue in the final solidified ingot. Most experimental methods applied to date have been poorly suited to study the complex dynamic fields associated with these convective phenomena. In this work, the novel technique of Molecular Tagging Velocimetry was extended and applied to investigate the transient velocity fields present during the uni-directional solidification of a transparent alloy analog (ammonium chloride). The whole-field two-component velocity map near the mushy layer and above the chimney, where lighter fluid rises, was measured at different times during the solidification process and at different locations. The mushy region exhibits a maximum velocity of order 1mm/s in both components while the plumes have a maximum velocity of order 7mm/s in the upward component. The measured velocity fields are expected to enhance understanding of the diverse transport phenomena present during the solidification process and provide quantitative verification of future computational analysis.

# DEDICATION

This thesis is dedicated to my parents who have been so supportive of me during my entire academic career.

ACKNOWLEDGEMENTS

It is a pleasure to have been working under the supervision of Dr. Manoochehr Koochesfahani who has taught me many things over the last two years. I thank him and other members of my committee; Dr. John J. McGrath and Dr. Andre Benard, whose advice and assistance have proved to be invaluable. I would also like to extend my gratitude to Doug Bohl, who has taught me many things during my stay in the lab and Frederic Boudesseul, whose help made the completion of this project possible.

This work has been made possible with funding from the National Science Foundation under Grant No. CTS-9901040 and made use of shared facilities of the MRSEC Program of the National Science Foundation, Award No. DMR-9809688.

TABLE OF CONTENTS

LIST OF TABLES

LIST OF FIGURES

LIST OF SYMBOLS AND ABBREVIATIONS

$\delta y$ - y component of displacement error

$\delta x$ - x component of displacement error

$\delta q$ - error in displacement magnitude

$\theta$ - grid intersecting angle

$\mu$ - micro

CCD - Charged Coupled Device

FOV - Field of View

Hz - Hertz

K - kilo

min - minutes

$m_{CD}$ - mass of cyclodextrin

$m_{h_2o}$ - mass of water

$m_{MTV}$ -mass of MTV chemicals

$m_{NH_4Cl}$ - mass of ammonium chloride

$M$ - Molar

MTV - Molecular Tagging Velocimetry

MSU - Michigan State University

$NH_4Cl$ - ammonium chloride

RMS - Root Mean Squared

S/N - Signal to noise ratio

s - seconds

TTL - Transistor - Transistor Logic

$V_{alcohol}$ - volume of alcohol

VD - Vertical Drive

# CHAPTER 1

# INTRODUCTION

Uni-directional solidification presents a unique method in the cooling of metals due to the increased resistance to creep and improved thermal fatigue behavior of the resultant cooled solid. However, the cooling orientation greatly influences the resultant imperfections within the product. In a side cooled casting, imperfections in the form of slanted rods known as A- and V- segregates form, while in a bottom chilled procedure, as utilized in this study, longitudinal channels oriented parallel to the direction of gravity form (Magirl and Incropera (1993)). These defects translate to the formation of a weaker material thus providing an impetus to the current research project.

Previous researchers used a myriad of techniques to better understand the convective mechanisms present during solidification and which cause the imperfections to occur. Magirl and Incropera (1993) used a dye visualization technique to track the flow of inter-dendritic fluid exiting the channels and also particle tracking to further reveal flow patterns within the melt, while Chen and Chen (1991) used a computer tomography technique to determine the porosity of the mush. Hellawell (1987) and Hellawell, Serazin and Steube (1993) conjectured that the onset of plume convection is caused by finite amplitude disturbances in the boundary layer at the mush-liquid interface. The onset of plume due to instabilities in the mushy layer is reinforced by linear stability theory (Worster, 1992).

Past experimental, analytical and numerical studies have established that the convective phenomena present can best be described in terms of complex dynamic velocity fields. Most experimental methods applied to date have been poorly suited to

accurately measure these phenomena and does not provide for whole-field measurements of the velocity (Chen et. al., 1991; Hellawell et. al., 1993; Magirl et. al., 1993; Prescott et. al., 1996; Beckerman et. al., 1996). One implementation of whole field measurements of the velocity was performed using PIV (Wang et. al., 1998) but the density gradients within the fluid itself may have made it difficult to select an appropriate seed particle. A recent effort at Michigan State University (MSU) utilized a novel technique called Molecular Tagging Velocimetry (MTV) in which a molecular tracer was used to non-intrusively measure the velocity fields above the mush using single line tagging that yielded one-component velocity measurements of the plume (Wirtz, et. al, 1998).

The first attempt at measuring the velocity of the plume at Michigan State University was meant to gauge the capabilities and application of the MTV technique in measuring velocity fields within an aqueous ammonium chloride solution. It was shown that the MTV technique is well suited to perform measurements on these scales. The present study attempts to extend the previous effort and provide comparisons and experimental validation for a future numerical simulation in the study of convective mechanisms of small-scale flows measuring velocities on the order of mm/s. Measurements were performed of the transient velocity fields above the mushy zone and in and around the plume where lighter fluid is rejected from within the solid mush during the uni-directional solidification of a transparent metal analog (ammonium chloride, $NH_4Cl$). Many researchers (Magirl and Incropera (1993), Beckermann and Wang (1996), Chen and Chen (1991)) use ammonium chloride in their study of convective mechanisms as it is a low-temperature analog of metal alloys and its transparent nature allows for optical access. The velocity fields obtained are expected to provide insight into the

porosity of the mush in future numerical analysis as part of the overall goal of our research group.

The better understanding of the convective mechanisms present during the solidification of a binary alloy would lead to the creation of a stronger alloy. In an effort to quantify the velocity fields within these convective mechanisms, two methods were utilized to study the solidification process, one being quantitative and the other qualitative. An adapted shadowgraph technique was used as a means of obtaining a visual picture of the process, from the formation of finger-like instabilities during the early stages, to the formation of plumes at later stages of the solidification.

The second method, Molecular Tagging Velocimetry (MTV), was utilized to obtain instantaneous velocity field measurements of the flow field above the mushy zone and above the chimney. The current study improves on the results of the previous work with the use of a two-component measurement and an improvement of the spatial resolution and data density by a factor of two.

# CHAPTER 2: EXPERIMENTAL PROCEDURE

## 2.1: Unidirectional solidification and Experimental Setup

This study explores the convective mechanisms present during solidification by way of unidirectional cooling of a fluid from the bottom. A hypereutectic aqueous ammonium chloride solution (26% weight percentage) was used which is known as a popular metal analog to metal alloys (Liu et. al. (1999), Wirtz et. al. (1998), Beckermann et. al. (1996)).

### 2.11 Details of Ammonium Chloride

Ammonium chloride is a popular low temperature analog due to the transparent nature of the fluid that allows for optical access. Also the temperature range at which solidification occurs provides a means for studying the convective mechanisms present in metal alloys. The equilibrium diagram for ammonium chloride is shown in Figure 2.1.1 where the dashed lines indicate the initial concentration and the final equilibrium temperature of the aqueous ammonium chloride used in the experiment while the dot above the liquidus line indicates the initial starting conditions. A detailed calculation for the preparation of the aqueous solution and the molecular tracers used in this experiment is provided in Appendix A.

The aqueous ammonium chloride solution was initially kept at 23°C. Once cooling of the fluid commences, the temperature of the fluid decreases with no change in concentration until the liquidus line is reached. The process will continue along the liquidus line, which implies that as the fluid gets cooler, ammonium chloride crystals precipitate out of the solution since the weight percentage of the fluid has to reduce to

maintain equilibrium. This process continues until the fluid reaches a temperature of -14°C (above the eutectic solid line). Limiting the minimum temperature that the fluid achieves prevents the solidification process from forming an eutectic solid and simplifies a numerical simulation.

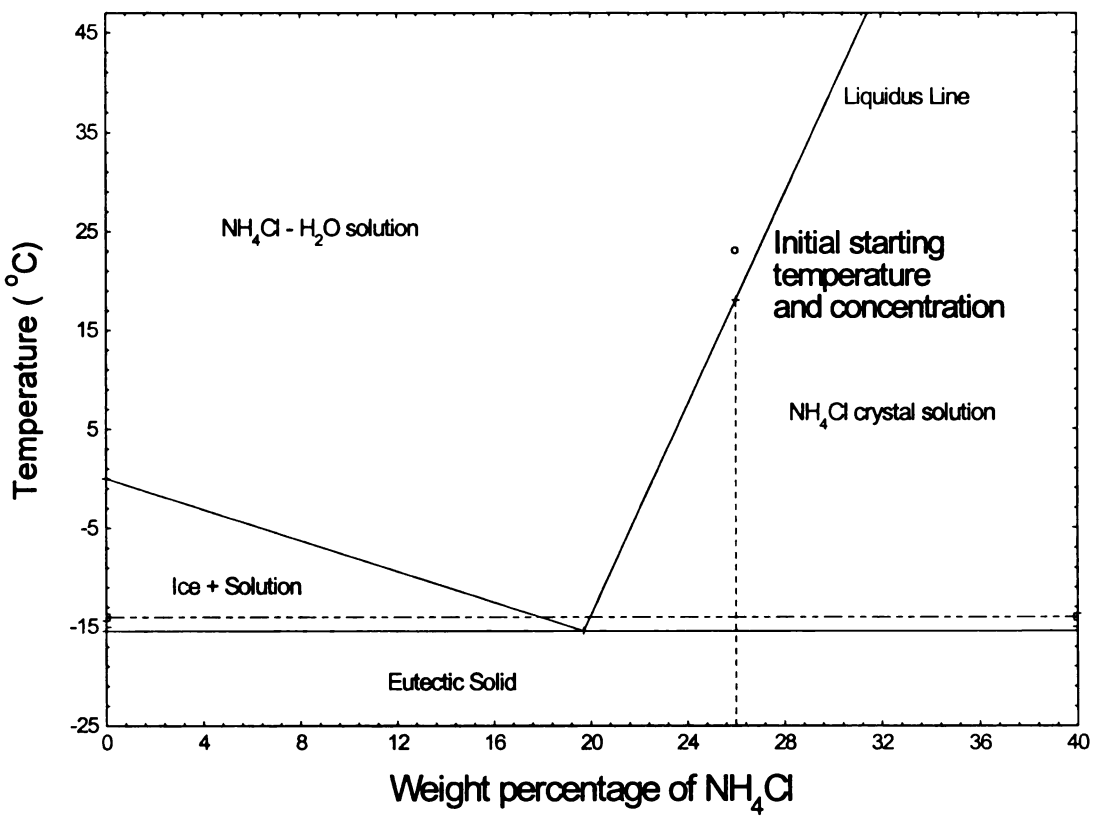


Figure 2.1.1 Equilibrium diagram of ammonium chloride.

During the cooling of the aqueous ammonium chloride solution, a vertical temperature gradient is established within the salt solution. This temperature gradient causes a stable density gradient to occur and results in a buoyancy force. As the ammonium chloride concentration near the mushy zone decreases due to the precipitation of ammonium chloride when the temperature is reduced, a solutal buoyancy force is established within the mushy zone, which is opposed to the buoyancy force induced by the temperature gradient. However, the solutal buoyancy force becomes a dominant

factor despite the presence of the stabilizing thermal force. This then causes large-scale convection to be induced in the bulk fluid.

### 2.1.2 Experimental Setup

A schematic of the test section used to conduct experiments is shown in Figure 2.1.2. The solidification system utilized is similar to the one described in Magirl and Incropera (1993) and is a modified version of a setup that was originally designed and used by Wirtz et. al (1998).

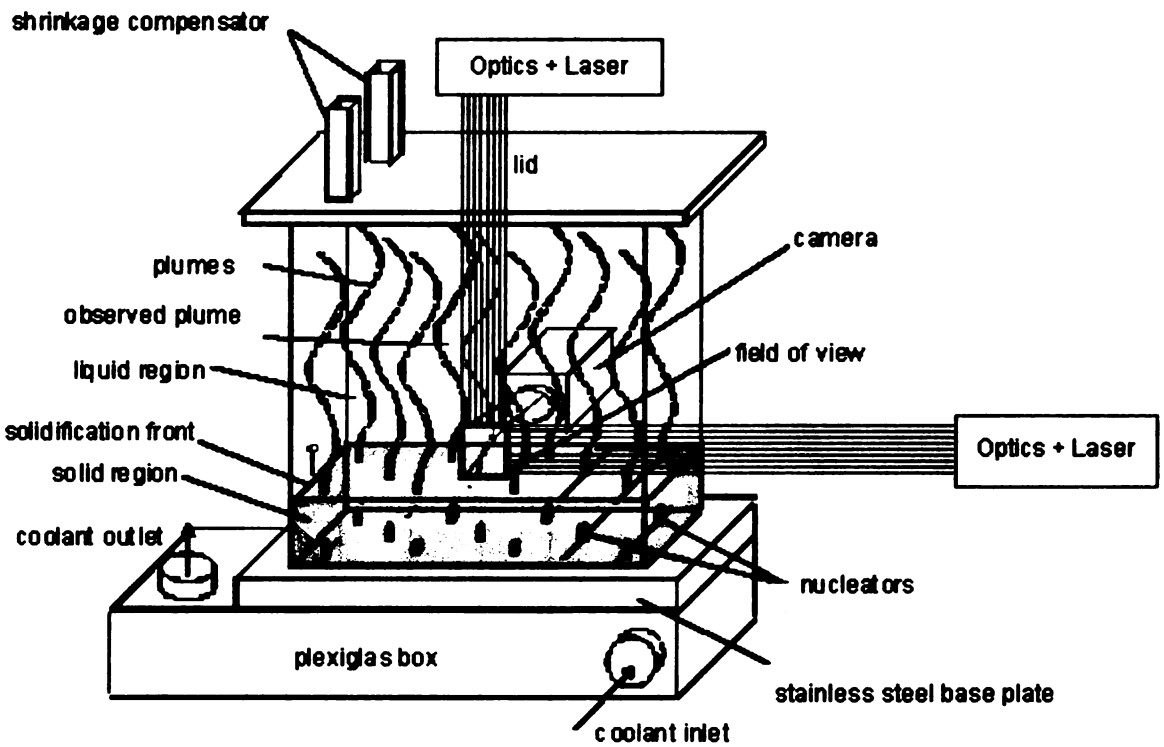


Figure 2.1.2. Schematic of test section.

The cooling of the fluid within the test section is achieved with the use of a base stainless steel plate as a heat transfer medium, which is exposed to a coolant bath on one side to provide for the cooling and aqueous ammonium chloride on the other within the

test section. An enclosure made of 1/4" quartz glass measuring 52 *x* 89 *x* 100mm was placed over the stainless steel base plate and sealed with high vacuum grease and gaskets to form the test section. Quartz glass was used due to the fact that it absorbs very little of the laser energy and thus is suitable for the transmission of laser beams and results in less attenuation.

During initial experimental trials, it was observed that convective plumes due to the density instability develop within the test section in a random manner. However, each experimental trial would yield approximately 11 chimneys within the test section. To better predict the location of these chimneys, 11 square nucleators were embedded in a regular manner in the base stainless steel plate to induce finite disturbances to the formation of the mush, which would allow the channels to form at those approximate locations. A schematic of the stainless steel plate and the coordinates of the stainless steel nucleators are provided in Figure 2.1.3.

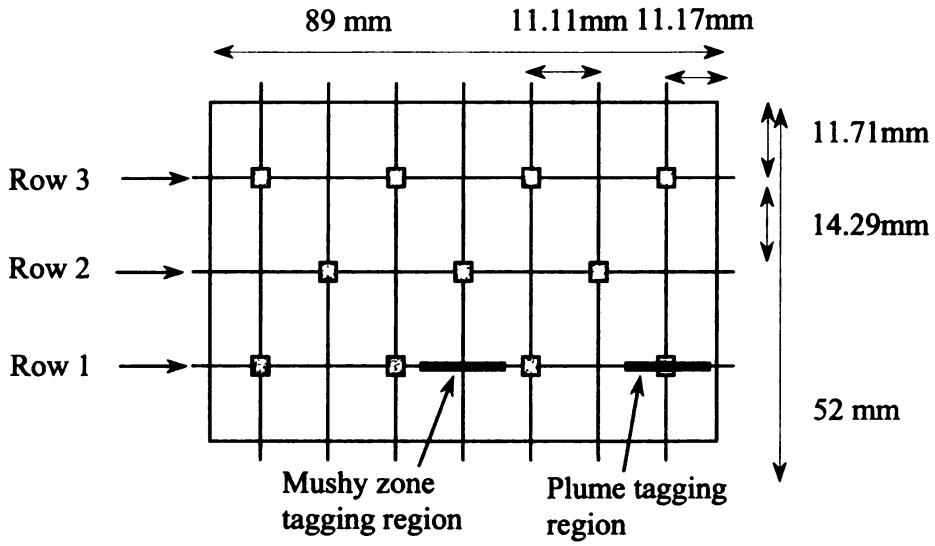


Figure 2.1.3. Schematic of base plate and embedded rectangle nucleators (shaded grey)

Experiments with and without the nucleators were performed to study the effects on the solidification process of adding nucleators to the base plate to control the formation of the plumes. No significant effect was discernible and the growth of the mushy zone with respect to time remains consistent with experiments done without the use of nucleators.

To ensure that the nucleator positions remain fixed within the test section and do not change between experiments, the nucleators were shaped so that an additional round base protrudes below the nucleator. The round base is embedded into the base stainless steel plate and glued-in with Loctite© Black Max glue. Figure 2.1.4 shows the schematic of the nucleator.

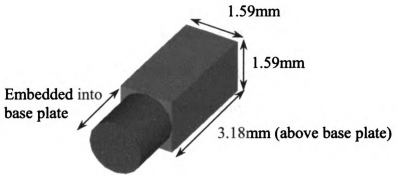


Figure 2.1.4. Schematic of nucleator

The nucleators act to induce the formation of channels associated with the rejection of buoyant fluid from the mushy zone. By fixing the arrangement of the channels in a regular manner by the use of nucleators, the formation of plumes is predictable - facilitating optical data acquisition for velocity measurements using MTV.

The stainless steel base plate is attached to a cooling chamber made of Plexiglas (see Figure 2.1.2). The cooling chamber has an inlet and outlet to allow the cooling fluid to pass. The cooling fluid used is a 50% mix of water and generic automotive anti-freeze

which is refrigerated by an external cooling bath (Neslab, RTE-140) and pumped through insulated tubing into the cooling chamber. To reduce the heat transfer to the surroundings, the cooling chamber was covered with weather strips. The cooling provided to the test section would then initiate the crystallization process.

Once the quartz enclosure is placed above the stainless steel plate, the test section is filled with a binary alloy; a hypereutectic (26%) ammonium chloride. A Plexiglas lid is then placed over it to seal the test section. Shrinkage compensators were fitted on the lid to allow additional fluid to be supplied during the experiment to compensate for solidification shrinkage. A window made of quartz glass was also fitted to allow penetration of the laser lines from the top.

However, this setup proved to be inadequate due to the amount of condensation that forms on the outer quartz walls whenever an experiment was performed. This is currently partially circumvented by running the experiments on low humidity days only, which highly restricts the progress of this work.

## 2.2 Details of Molecular Tagging Velocimetry

### 2.2.1 MTV Chemicals

A phosphorescent compound used in the MTV technique was added to the aqueous ammonium chloride solution to serve as molecular level tracers. When excited with an excimer laser (308nm), these tracers emit light that has a lifetime of ~5ms. A grid pattern created with the laser would be imaged at two successive times within the lifetime of the tracer to capture two consecutive images. The two images are correlated to obtain the velocity vectors and thus the velocity field measurements.

A molecular complex is suitable for molecular tagging applications if its lifetime as a tracer is long enough relative to the flow convection time scale to allow sufficient displacement of the tagged regions. The MTV technique has successfully been applied to the characterization of a variety of flows at the Turbulent Mixing and Unsteady Aerodynamics Laboratory at Michigan State University including the flow field measurement within an internal combustion engine, the wake of an unsteady airfoil and vortex flows and it is now being used for small-scale applications in the solidification of an alloy. The MTV Triplex consists of a lumophore, 1-Br-Np; an alcohol, cyclohexanol; and a sugar, cyclodextrin; and is collectively known as 1-BrNp-Gβ-CD•ROH. The concentrations of the MTV triplex used in this study are $2 \times 10^{-4} M$ for Gβ-Cyclodextrin, $0.06M$ for alcohol and a saturated amount of bromo-napthalene was added (Gendrich et. al., 1997).

The MTV technique involves mixing a tracer into the ammonium chloride solution. Therefore the presence of the tracer could potentially affect the solidification by changing the crystallization process, the thermal behavior or the flow behavior. The typical concentration of the ammonium chloride solution is 26% by weight, whereas the highest concentration of the three components of the MTV triplex is less by at least three orders of magnitude (in molar concentration). Due to the small concentrations of the tracer used, it is expected that the physical properties do not change significantly, so that the thermal and flow behavior of both systems with and without the tracer would be equal. To confirm this, experiments with and without using the tracer were performed. A comparison between the experiments did not indicate any change in behavior including the temperature range in which crystallization commenced or the development of the

mushy zone. Thus, the solidification and convective behavior were not noticeably influenced by the presence of the tracer molecules.

During initial experimental trials, it was observed that the phosphorescence of the tagged field of view appears brighter than tagged field of views of conventional applications of MTV within water and yielded longer delay times between the undelayed and delayed images. This prompted the investigation of the lifetime of the mixture of aqueous ammonium chloride and the MTV chemicals to determine how the addition of ammonium chloride to the solution has affected the lifetime values. The lifetime of the MTV Triplex in the presence of different concentrations of ammonium chloride was determined and the results are shown in Figure 2.2.1.

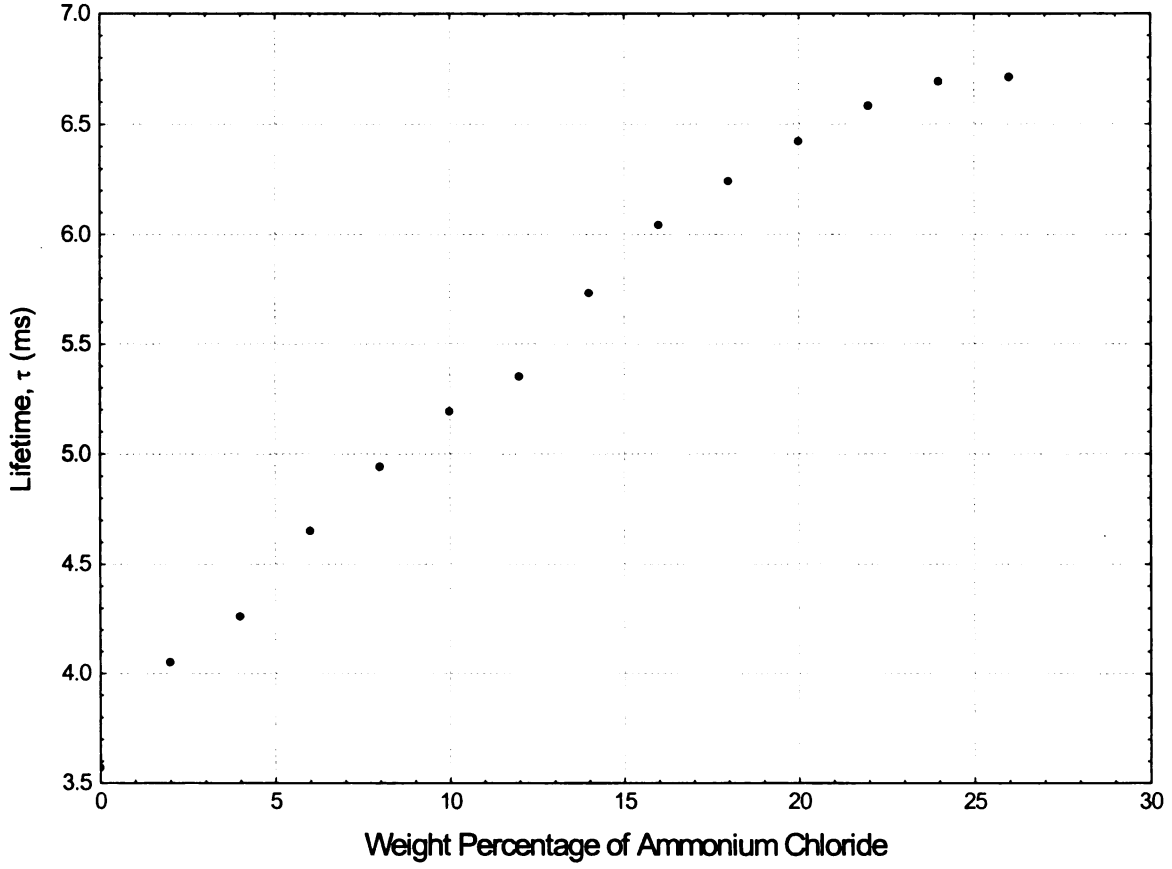


Figure 2.2.1. Plot of lifetime as a function of weight percentage of ammonium chloride + MTV chemicals (Cyclohexanol)

In the figure, it can be seen that the lifetime value without ammonium chloride matches the previously published lifetime value of the MTV triplex of ~3.7ms at the same mixture concentration (Gendrich et. al., 1997). By adding ammonium chloride to the MTV solution, it can be seen that the lifetime increases significantly before tapering off at ~ 6.7ms. At this point, the weight percentage of ammonium chloride present in the solution (~20-25%) is approaching the saturation limit of ammonium chloride solubility. Due to the increased lifetime of the molecular tracers in the presence of ammonium chloride, longer time delays and thus measurements of slower velocities are possible. It is theorized that the presence of ammonium chloride shields the molecular tracers from being quenched after tagging by the laser lines.

However, it should be noted that lifetime is measured as the time when the intensity drops to $e^{-1}$ of the original intensity. Measurements can still be made at longer time delays with the use of proper detectors, which in this case is an image-intensified camera. Using delays in the range of 50-60ms, the MTV Triplex alone would not yield enough light to capture the delayed image when the intensity would have dropped to approximately $e^{-16}$ of the original intensity. It is through the presence of ammonium chloride, which allows the intensity to be raised to approximately $e^{-9}$ of the original intensity, and the use of an image intensified camera that it is possible to measure such slow flows. More details of the MTV triplex can be found in Gendrich, et. al. (1997).

### 2.2.2 Optics Setup

Creating the appropriate tagging pattern for velocity measurements involves an elaborate setup of optics. During the setup, many lenses were used to manipulate the laser

beam. To illuminate the field of view effectively, we need to make a laser sheet that is as thin as possible in the physical world so that the tagged field of view is planar. Thinning the laser beam requires an accurate setup of optics and how thin it can get is limited by the diffraction limits of the optics.

To achieve this, a 20ns, 100mJ/pulse beam from an excimer laser (Lambda Physik LPX 220 iCC filled with XeCl) was initially passed through a VFL (Variable Focal Length) setup consisting of a 150mm and 50mm cylindrical lens to increase the aspect ratio. This, in effect, reduces the outgoing rectangular laser beam from the laser to a thin sheet that is less than 1mm thick. The optics setup is illustrated in Figure 2.2.2.

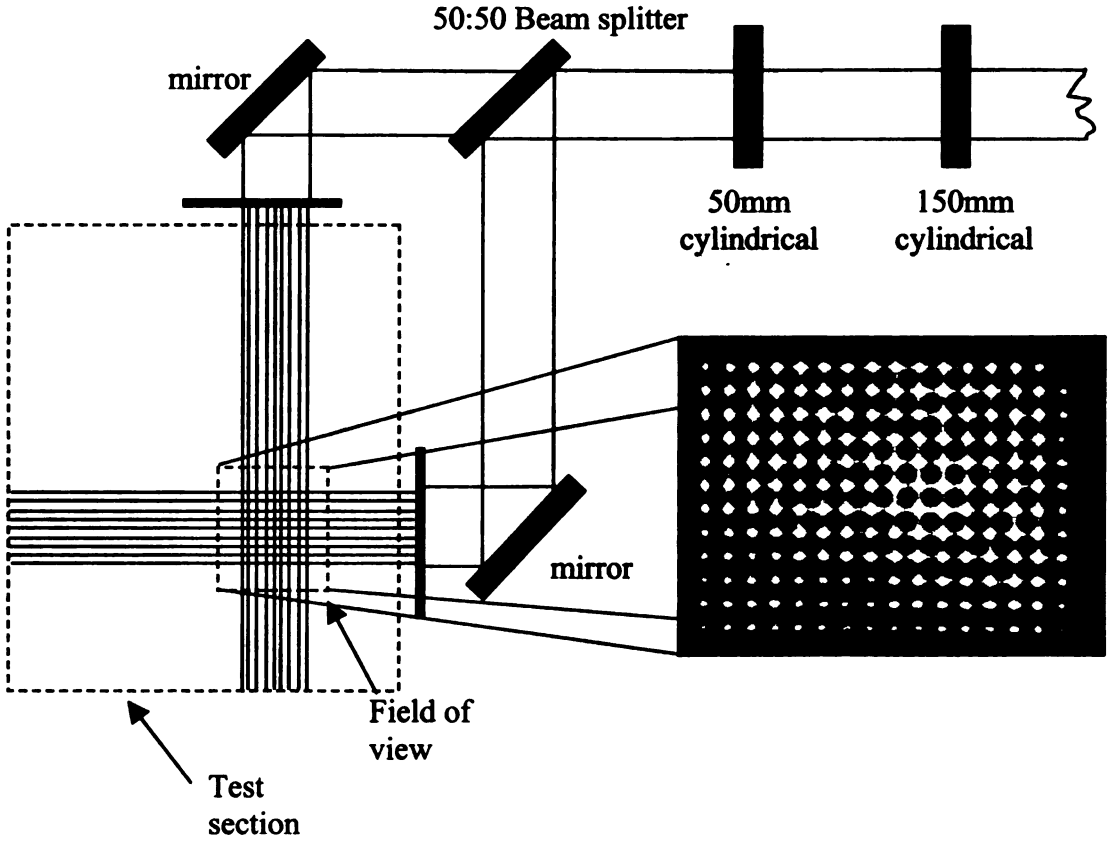


Figure 2.2.2. Optics Setup

To achieve two intersecting laser lines, the main laser beam is split into two using a 50:50 beam splitter. After this, the laser sheet is basically reflected using mirrors and passed

through beam blockers to create the intersecting grid pattern. The optics setup in Figure 2.2.2 was used to measure the flow field near the mushy zone where the velocities are slow - on the order of 1mm/s. In a field of view of ~14mm *x* 10.5mm, a total of 192 intersections were achieved with 12 horizontal and 16 vertical laser lines at a 90° intersection. This corresponds to a spatial resolution of 775μm for the velocity measurements above the mushy zone. The field of view just mentioned corresponds to a 1.6:1 image ratio since the CCD array size is 8.8x6.6mm.

In designing the beam blockers, the goal was to create an array of slots that are very thin in order for the smaller features within the flow field to be resolved. However, due to equipment limitations, the smallest slot achievable was 0.015cm (0.006") with a spacing of 0.058cm (0.023"). A schematic of the beam blocker is shown in Figure 2.2.3.

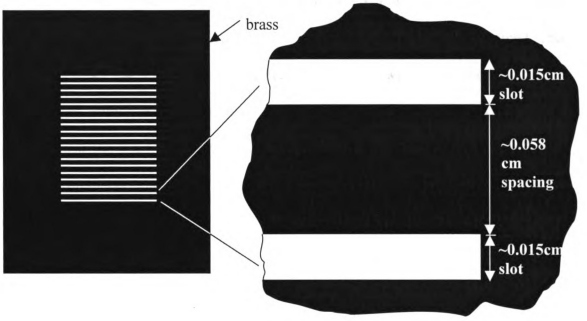


Figure 2.2.3. Beam blocker design

If the slots or spacing between them were cut any smaller, warping would occur and the beam blockers would yield non-uniform laser lines. This area could be improved upon in the future by employing more cutting edge machinery or chemical etching to create thinner slots.

In previous experiments, it was found that as the mushy zone grows and nears the grid pattern, the intensity of the lower laser lines closest to the mushy zone increases due to the lower temperature present, causing the image to saturate. Reducing the gain causes the upper lines farther from the mushy zone to be too dark for correlation. Thus the lower laser lines (closest to the base plate) were intentionally made to be less intense so that as the mushy zone nears the grid pattern, the image is still below saturation while maintaining sufficient signal to noise ratio over the whole image. One concern in irradiating the flow field with a laser is the potential heating of the fluid. The heating effect of the laser was calculated and a temperature rise of less than 0.09K/pulse (worst case where all the energy is absorbed) over the whole field of view was determined. This is negligibly small and is not expected to affect the flow field within the bulk fluid.

Images from three fields of view were acquired at different times to capture the flow field near the mushy zone. Figure 2.2.4 shows the location of the fields of view where measurements were performed. Each field of view covers an area of ~14.5 $x$ 10.5mm with the bottom of each field of view being y = 10.5mm, 21.0mm and 31.5mm respectively from the base plate.

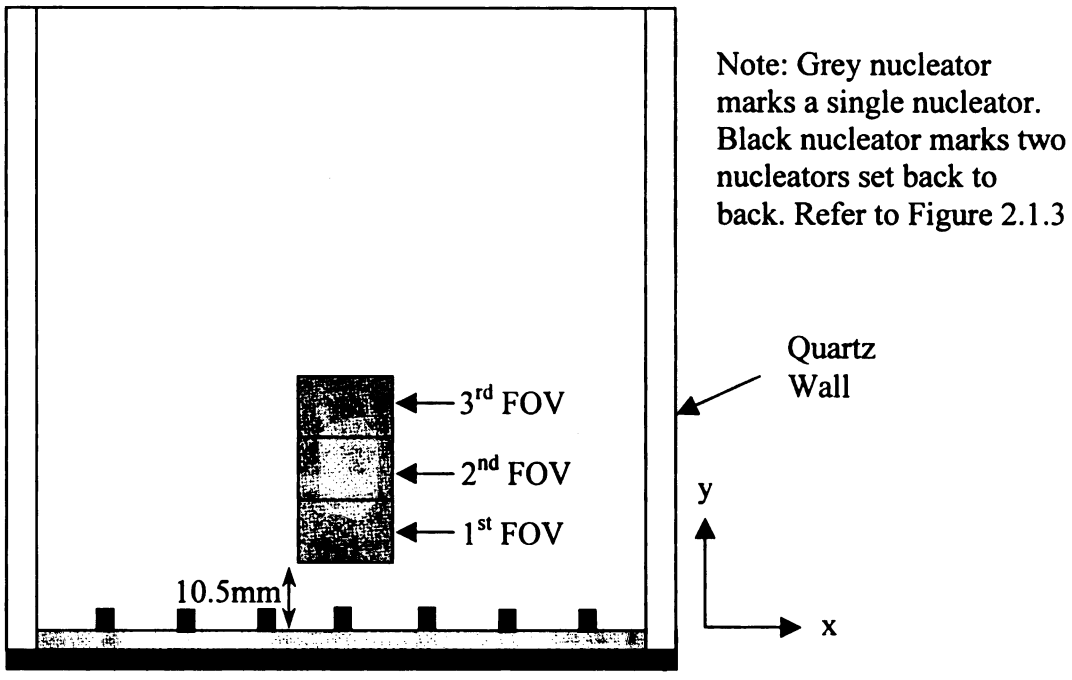


Figure 2.2.4. Measurement field of views for mushy region

Note that the measurements made above the mushy region are located between two nucleators where no plumes would form. The field of views are located on the same plane as Row 1 (refer to Figure 2.1.3 for row designations) and the nucleator in this region is located on Row 2. However, the grid pattern used for measurements in the mushy zone could not be applied to measurements of the plume. As the plume rises vertically, the edges of the plume causes the vertical laser lines to refract and result in a "fuzzy" pattern in certain areas of the image, which may not correlate well. An example of a refracted grid line is shown in Figure 2.2.5.

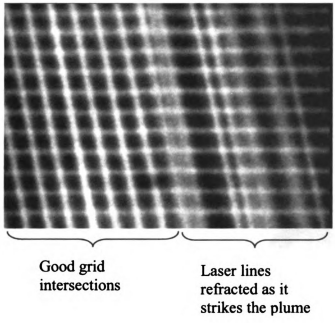


Figure 2.2.5. Refracted laser lines for plume measurement

To circumvent this difficulty, the optics setup was rotated by an angle of ~ 45° so that the laser lines penetrate from the side of the quartz test section. By having the grid pattern intersect the plumes from the side, the possibility of having the laser lines refracted by the rising plumes would decrease and thus produce better quality images that correlate better. However, when the laser lines penetrate the side quartz walls at an angle, the spacing between the laser lines increases and causes the grid density to decrease, thereby lowering the data spatial density. The spatial density of the measurements is 960μm. Future considerations to improve the data spatial density are to utilize an additional lens of the appropriate focus length to focus down the beam and reduce the width of the laser lines and also the distance between them. Beam blockers with smaller slots would also contribute to increasing the data density.

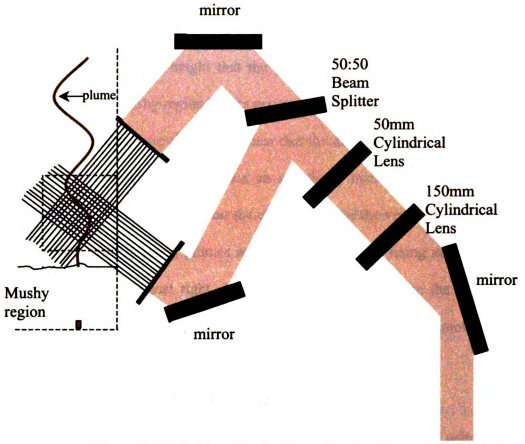


Figure 2.2.6. Schematic of optics setup for plume measurement

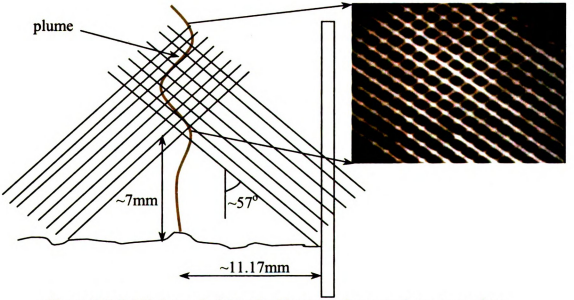


Figure 2.2.7. Minimum height of grid pattern from mushy zone surface

The schematic of the modified optics setup is provided in Figure 2.2.6.With this setup, the bottom of the grid pattern is always at a distance from the tip of the chimney. Figure 2.2.7 shows the minimum height that the grid pattern would be able to approach the chimney before the mushy region blocks penetration to the laser line.

From the schematic above, it is clear that the diagonal grid pattern can only be as close as ~7mm to the chimney. Thus an additional method needs to be devised to measure the plume velocity very near the chimney. Since the vertical laser lines could not penetrate the vertically rising plumes and the fluid is mainly rising vertically, horizontal laser lines were passed just right above the chimney to measure the V-component of velocity using simple line tagging, before the plume takes on a helical motion.

### 2.2.3 Correlation of MTV images

The images obtained from the experiments were correlated using an in-house correlation code written in C. This was developed at the Turbulent Mixing and Unsteady Aerodynamics Laboratory (Gendrich et. al., 1997). To ensure that the displacements obtained from the correlation are physically meaningful, a scale image needs to be obtained after each experiment. This scale image acts to rescale the data from the original pixel units to physical units and thus yield velocity measurements in mm/s.

The measurements obtained need to be placed onto a regular grid as the original MTV grid is most likely arranged in an irregular fashion. A local least squares fit of a $2^{nd}$ order polynomial was performed on the irregularly spaced velocity points. In using the second order polynomial fit, a minimum of 6 and a maximum of 8 surrounding velocity points were used to remap a single velocity data on the regular grid. When the velocity

data are remapped onto a regular grid, the grid spacing is kept to be approximately the same as the average grid spacing in the original MTV grid so that the data density in the irregular grid is the same after remapping it onto a regular grid. The accuracy of the remapped data is discussed further in Cohn et. al. (2000).

In the measurements of the mushy region, the laser lines were orthogonal with respect to each other and thus the errors in the estimated $x$- and $y$- components of the displacement vector ($\delta y$ and $\delta x$) in the correlation procedure are comparable. However, as the intersection angle increases, as in the case of measurements above the chimney, $|\delta x|$ values decrease at the expense of increasing $|\delta y|$. As expected, in the limit of the grid intersecting angle, $\theta = 180^{\circ}$, the determination of $\Delta y$ becomes ill posed (Gendrich et. al. 1996).

Based on the results published in Gendrich et. al. (1996), at intersection angles of less than $130^{\circ}$, the error in the $y$ displacement and image signal to noise ratio (S/N) of better than 4 should produce displacement estimates with better than 0.1 pixel accuracy in both the $x$- and $y$- directions. Figure 2.2.8 is taken from Gendrich et. al (1996) which illustrates the accuracy expected from the correlated images with tagging patterns at different intersecting angles.

Most of the data yielded a S/N ratio of 8 and an intersection angle of $\sim 110^{\circ}$. This translates to a displacement uncertainty of less than 0.05 pixels which in physical units relates to velocity measurements with an uncertainty of $\pm$ 0.02mm/sec within the plume. Measurements above the mushy region would result in a slightly higher accuracy due to the orthogonal intersection. The displacement uncertainty corresponds to a 95% confidence level, which implies that 95% of the computed displacements have errors less

than or equal to the displacement uncertainty. This is a more conservative measurement compared to the RMS value. If the error distribution is Gaussian, then the RMS error estimate is $\delta q)_{RMS}=0.5(\delta q)_{0.95}$

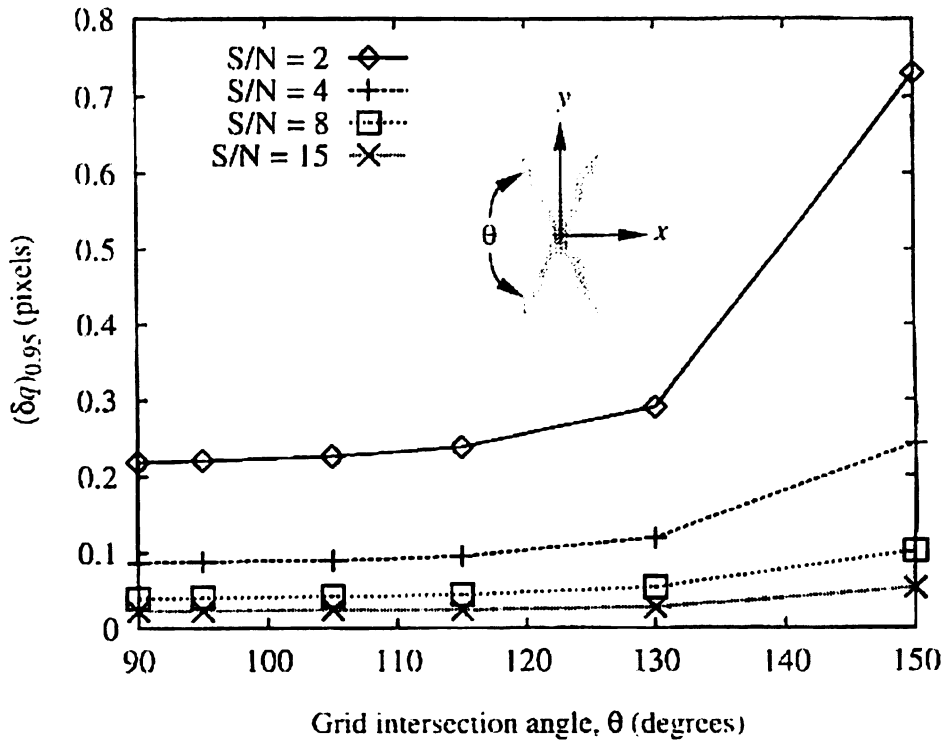


Figure 2.2.8. Displacement sub-pixel accuracy versus θ for different values of S/N (Gendrich et. al., 1996)

Another aspect that warrants discussion is the effect the intersecting angle has on the individual component displacement errors. This is illustrated in Figure 2.2.9. It is apparent from Figure 2.2.9 that as the intersecting angle increases, the error magnitude in one component of the velocity measurement will increase accordingly (40% worse in one component in our case). In the measurements of the plume, the acute angle is in the x-direction and results in the x- component having a higher magnitude of error than the y-component. A more detailed discussion of sub-pixel accuracy and other correlation issues are provided in Gendrich et. al. (1996).

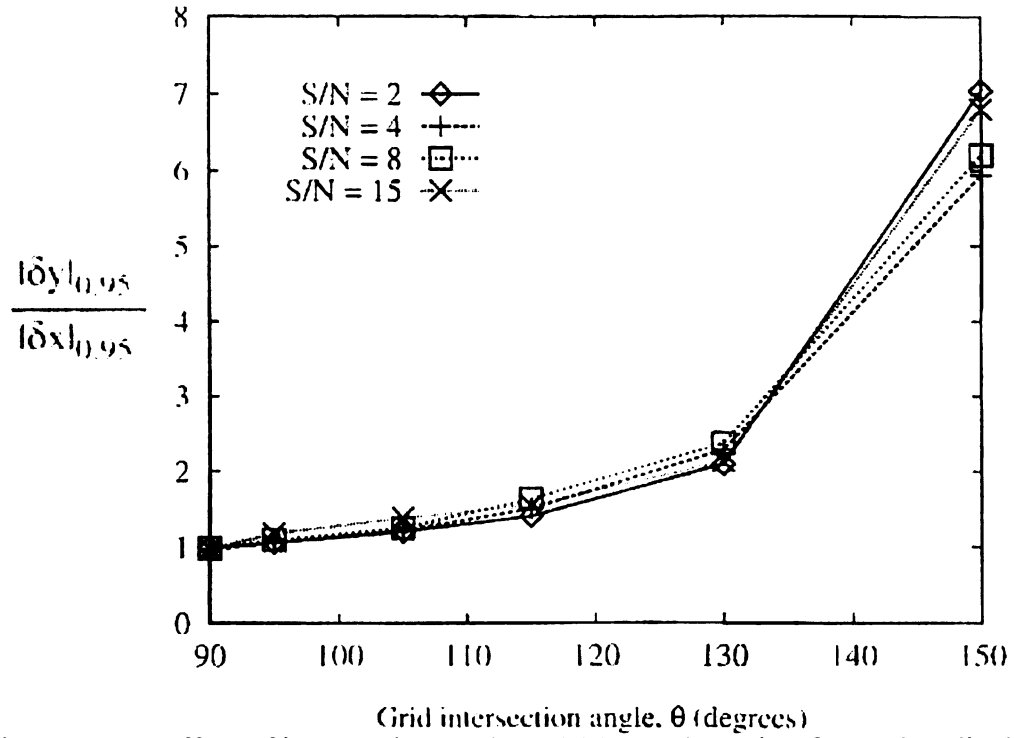


Figure 2.2.9. Effect of intersection angle and S/N on the ratio of $x$- and $y$- displacement error magnitudes.

## 2.3 Image Acquisition System

In imaging the fields of view, an intensified camera and various electronics were used in order to detect the tagging pattern in low light conditions. A 105mm Micro Nikkor ( $f$ / 2.8 ) lens with an additional close-up lens was used in conjunction with an intensified camera, a Xybion Gated Intensified CCD Video Camera (Model ISG-350) and the Video Camera Control Unit (Model CCU-01). To provide the electronically gated camera with a gate signal, a Stanford Research System, Inc. (SRS) Four Channel Digital Delay/Pulse Generator was used. Two TTL pulses were generated and combined using an "AND" gate and fed to the camera. The physical setup is illustrated in Figure 2.3.1.

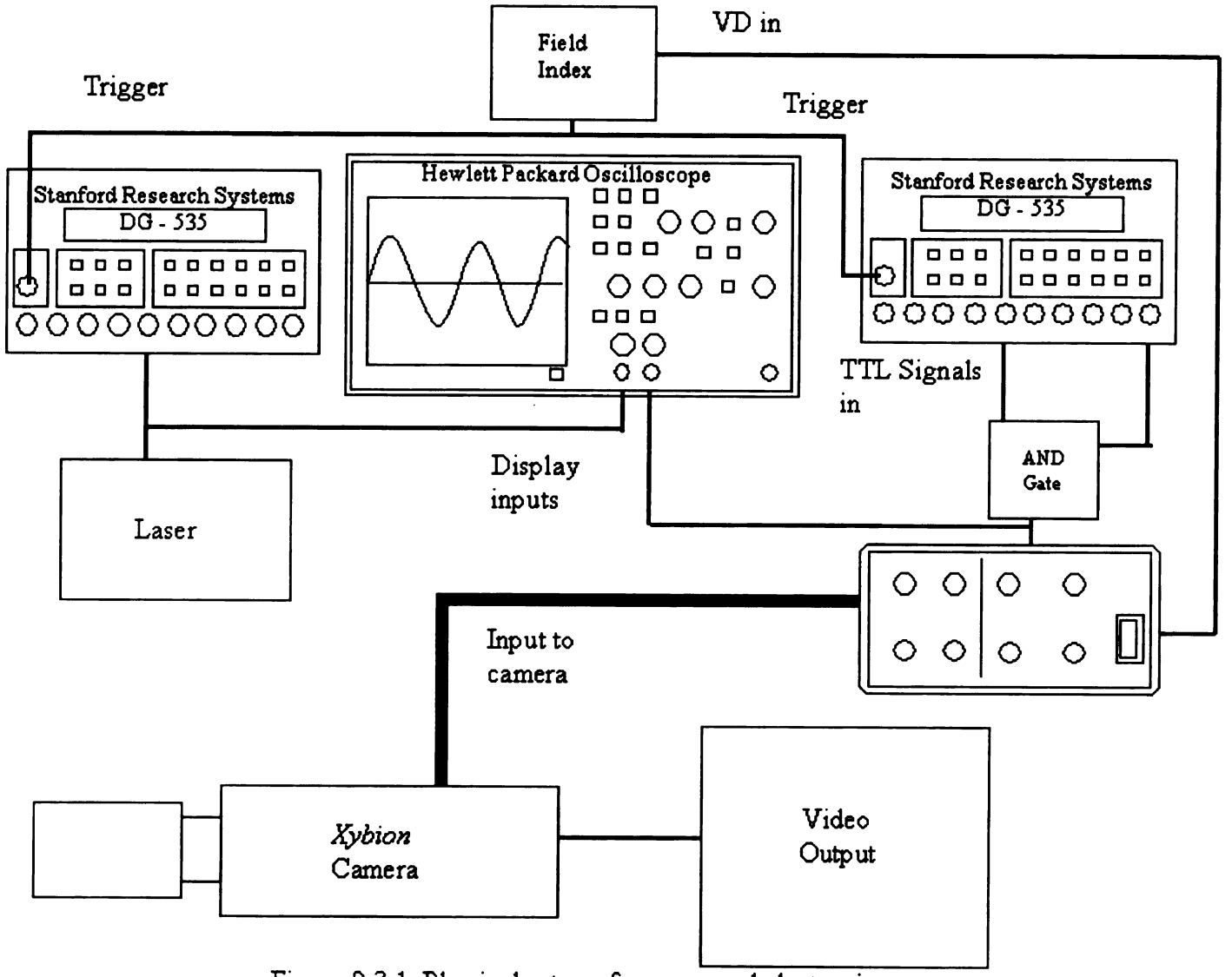


Figure 2.3.1. Physical setup of camera and electronics

Figure 2.3.2 details the input and output signals fed to the camera and laser for synchronization:

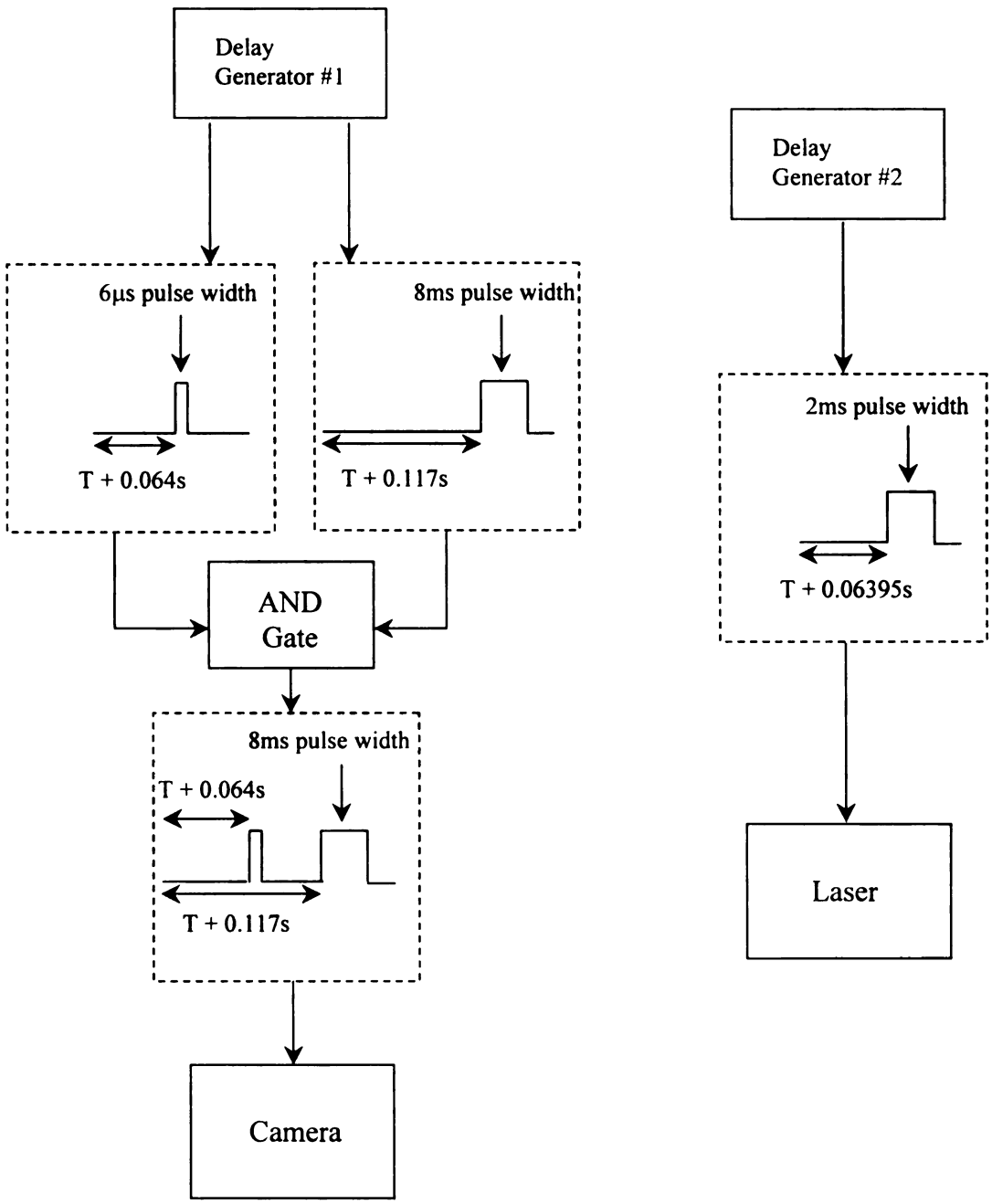


Figure 2.3.2. Schematic of typical timing used for gating the camera and laser

With reference to the timing diagram in Figure 2.3.2, the first gate (6μs) allows the camera to capture the undelayed image when the laser first fires while the second gate (8ms) allows the delayed image to be captured at a later time. In selecting the time delay between the delayed and undelayed images, two factors need to be considered, one being the range of timing which allows for full frame capture of the image and the other being the amount of light available for detection by the CCD.

The delay time used is constrained by the timing of the camera, which only enables double gating in a specific range due to the RS-170 standard utilized by the camera. In order for the two images (undelayed and delayed) to be captured in full frame mode, the gating signals need to be positioned within the field overlap so that both the even and odd fields would be exposed in that period to form a complete image. This is illustrated in Figure 2.3.3.

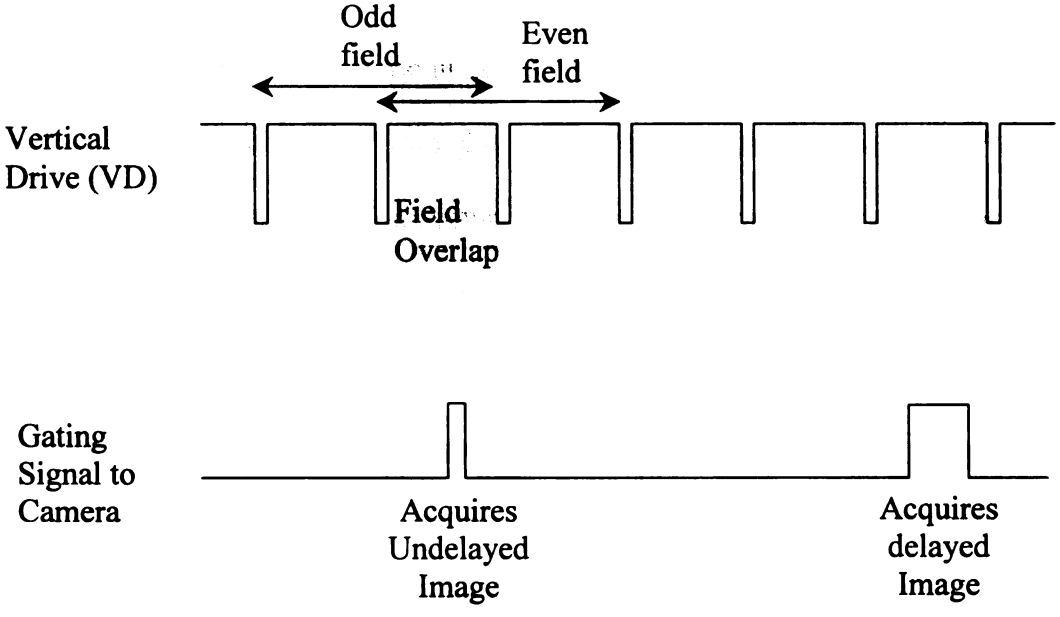


Figure 2.3.3. Schematic of gate signals with respect to the vertical drive of the camera

If the gates were positioned in either the odd or even field only and not in the overlap region, the image acquired would only show every other line, as the other field was not exposed to the field of view in the gate period. To measure the low speeds present in this experiment, the delay time between the undelayed and delayed image needs to be more than 50ms. Since the time between vertical drives is ~16.66ms, the two gate periods need to be separated by three vertical drives to attain that delay time. This is shown in Figure 2.3.3. Longer delay times (an additional 16.66ms) could not be used, as by then, there would not be enough light left to capture the image. Since the gating signals are separated by three vertical drives, one overlap period in between the undelayed and delayed image would be unshuttered. Thus there would be an empty frame in between each image captured, which reduces the acquisition rate by half. For every 60 images that were captured, 30 would be blank frames and of the other 30 remaining, half are undelayed and the rest delayed leaving 15 pairs for correlation.

The time delay between the undelayed and delayed image used is in the range of 54.995ms-56.995ms measured from the center of both gates. At a later stage in the experiment, when bleaching effects come into play, the gate period needs to be increased accordingly to allow sufficient light for image acquisition.

## 2.4 Experimental Procedure

One of the main concerns in any experiment is the proper characterization of the boundary conditions. In this experiment, it is found to be even more crucial since it is a temperature-based experiment and the surrounding temperature and humidity in our location changes with the season. Thus all experiments were completed in a very narrow

time frame to ensure that the boundary conditions remain essentially the same since the experimental setup did not take into account environmental changes.

Before starting the experiment, the Neslab external cooling bath was initially set to 23°C and the fluid circulated within the Plexiglas box (see Figure 2.1.2). This was done each time before the experiment to ensure that the base plate is always at the same temperature so that the operating conditions remain the same in between experiments. Any entrained air within the cooling box is evacuated to the external cooling bath by tilting the test section. After the coolant has been circulating within the cooling box for some time, the flow of fluid was impeded and the Neslab coolant bath was brought down to a temperature of -21.5°C.

The test section is then filled with aqueous ammonium chloride and sealed. Once the coolant in the Neslab coolant bath has achieved a temperature of -21.5°C, the valves were reopened to allow the experiment to commence. Since the flow lines and the cooling box were set to 23°C initially, the chilled coolant naturally experiences a drop in temperature when the flow is restored. This is taken into account by intentionally setting the temperature lower than the desired temperature of -18.6°C. When the flow is restored, the temperature of the external cooling bath drops a few degrees to around -18°C and the temperature was reset to -18.6°C which is the desired final temperature. This procedure reduces the time needed for the temperature of the base plate to reach -14°C.

Countless experimental trials and calculations done by Kay Wirtz in his thesis arrived upon the temperature value of -18.6°C. In the previous effort at MSU by Kay Wirtz, temperature measurements were made at different locations of the test section and

it was concluded that the base plate temperature would attain a value of -14°C if the coolant bath was set to a temperature of -18.6°C (Wirtz et. al, 1998).

One of the first experiments that were done was a visualization of the solidification process to provide a means for understanding the complex dynamic flow of a uni-directional solidification. In visualizing the convective plumes that develop during solidification, a Shadowgraph type visualization was utilized. This shadowgraph technique is slightly modified from that normally used by other researchers. Most shadowgraph techniques utilize a parallel light source from behind the interrogation area, which would project the shadow of the density gradients within the fluid onto a screen.

The method used here utilizes ambient room light for illumination and an alternating vertical black and white background to contrast the edges of the convective plumes. One of the main factors in this setup that allows the plume edges to contrast against the alternating black and white lines is the direction of the scattered light. If the test section was exposed to room light, the illumination from above the test section would be stronger than that from behind it making it difficult to discern the presence of the plumes. However, when the test section is enclosed so that illumination from above is impeded, the main illumination is from the back of the test section, which allows this technique to work very well. Another factor that needs to be considered in producing good image contrast is in the wavelength and the width of the alternating black and white lines placed a distance away from the test section. These lines were placed approximately 2 meters away from the test section and cover the whole background of the test section. Figure 2.4.1 illustrates the setup that was used in the visualization.

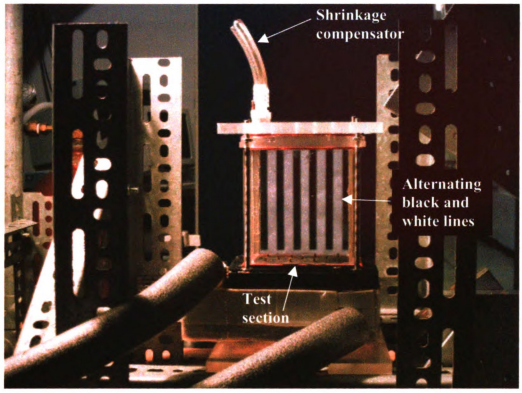


Figure 2.4.1. Setup for Visualization

When the images are taken, the width of these lines needs to be such that it is the same as the distance separating two adjacent plumes in the field of view. This in effect allows the edges of the alternating lines to coincide with the plumes and provide for the contrast necessary to discern the plumes. Other line widths and wavelengths were experimented with but these provided unsatisfactory results.

However, this method would display density gradients well only in the horizontal direction due to the edges of the plume being mainly in the vertical direction. Double diffusive layers are less obvious compared to the standard Shadowgraph technique although still very much visible. If the vertical alternating black and white lines were rotated to be in the horizontal direction, the vertical density gradient i.e. double diffusive

layers would be more obvious but sacrifices the ability to contrast the horizontal density gradients. Before starting the experiment, a reference image was taken of the test section. This was used to subtract out the background so that the images do not show the alternating black and white background. To acquire the images used for visualization, a Pulnix TM-1040 (1K x 1K) camera was used in conjunction with a Coreco data acquisition board.

In making whole field velocity measurements with the MTV technique, various aspects of the experiment need to be kept in check to ensure that the laser tagging process is unimpeded. The quartz test section needs to be exceptionally clean so that the laser penetrates the test section cleanly and does not cause reflection, which would deteriorate the image quality. In the process of aligning the laser beam, it is imperative that the laser beam is always "square" with the optics so that minimal reflection would occur and the shape of the laser beam is not distorted. In the event that the laser beam is not "square", the laser-tagging pattern may cause reflection within the test section or induce irregular illumination of the tagging field and cause a reduction in the signal to noise ratio.

# Chapter 3: Results and Discussion

## 3.1 Visualization

One of the first sets of data to be taken for this experiment was the visualization of the process from when the cooling starts to 2 hours into the solidification. The visualization serves as a means to better understand the flow phenomena present during the solidification process and also to illustrate the location where MTV measurements were made in this study. The method used to obtain high quality pictures was an adapted Shadowgraph method as described in Section 2.4: Experimental Procedure.

During the experiment, many time ticks were recorded which include images of the solidification process at 0, 2, 4, 6, 8, 10, 12, 14, 16, 18, 20, 25, 30, 35, 40, 45, 50, 55, 60, 70, 80, 90, 100, 110 and 120 minutes. At each time tick, 120 images were taken in a time frame of 20 seconds at an acquisition rate of 6Hz (Four frames are skipped for every frame acquired). Although the video sequence appears jerky due to the low acquisition rate, it is the only way to save disk space and have the ability to acquire a longer sequence. A longer sequence allows us to capture a more complete picture of the evolving plumes and other characteristics of the flow.

During the initial stages of cooling, rapid growth of the mushy layer indicated the presence of substantial fluid under-cooling. This results in the formation of many ascending water-rich fingers and the formation of ammonium chloride crystals, which would settle to the bottom of the test section to make up the mushy region. Figure 3.1.1 shows the regime of small fingers and the formation of the mushy region.

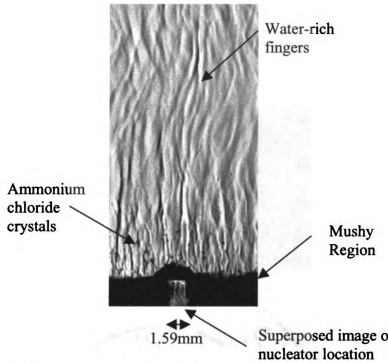


Figure 3.1.1. Small fingers and ammonium chloride crystals at 8 minutes into the solidification.

It is observed that at 4 minutes into the solidification process, small fingers start to form at the center of the base plate and can be seen rising, although they quickly lose their solutal identity and mix with the surrounding fluid. At 6 minutes, more plumes maintain their solutal identity and are able to traverse higher. Due to the large Lewis number of ammonium chloride, the water-rich fingers retained their compositional identity and were clearly visible to the top of the test section before they would begin to collapse. (Magirl and Incropera, 1993)

A substantial amount of ammonium chloride crystals can be seen falling from ~5mm from the mushy region due to the substantial fluid undercooling present just above the mushy region during the early stage. As solidification continues, the amount of ammonium chloride crystals descending onto the mush lessens but the fingers become

more vigorous and would sometimes advect small crystals upward into the flow field. A sequence of images is shown in Figures 3.1.2 to illustrate the evolution of the mushy region as well as the plumes.

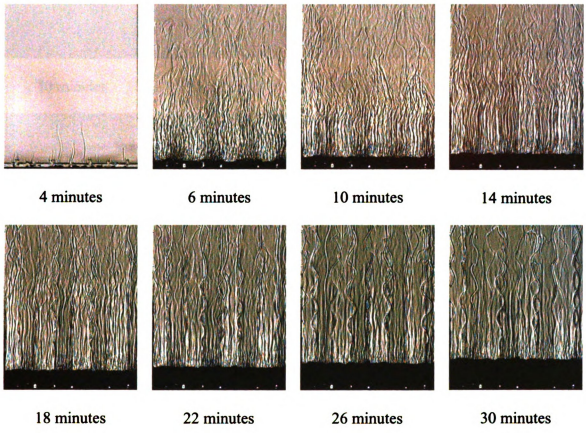


Figure 3.1.2. Images show visualization of solidification process from 4-30 minutes.

Notice that during the initial stages of solidification, water-rich fingers are manifest throughout the entire flow field. At ~18 minutes, stronger fingers start to appear that reach all the way to the top of the test section. As the plumes strengthen, surrounding fingers start to decrease in quantity as neighboring plumes compete for the supply of water rich fluid from within the mush. The strengthening of the plumes can be seen from 18 minutes to 30 minutes in Figure 3.1.2

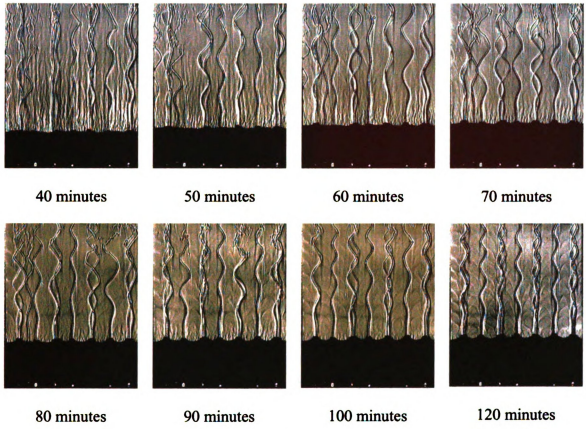


Figure 3.1.3. Images show visualization of solidification process from 40-120 minutes.

At around 40 minutes as illustrated in Figure 3.1.3, it becomes apparent that the plumes are developing above the nucleation sites although there are approximately 14 plumes at this stage compared to the 11 nucleators. At a later stage in the solidification process (~60 minutes), due to the finite disturbance induced by the square nucleators, most of the fingers have died down and consolidated into stronger plumes at locations where the nucleators are positioned. These plumes originate from within the mushy layer where lighter fluid is rejected due to the formation of the mush. At later stages of the experiment, double diffusive layers form, which are indicated by the horizontal diffusive interfaces at 90 minutes in Figure 3.1.3.

Small-scale fingers become less visible late in the solidification process and completely disappear at around 120 minutes. One point of interest can be observed at 70 minutes where plume buckling is visible at the top of the test section. However, the plumes seem to recover and take on a three-dimensional helical motion again later in time. Magirl and Incropera (1993) noted this phenomenon in their experiments and concluded that as the plume oscillated in its plane, fluid motion in the outer bends is retarded by viscous drag but as fluid continues to ascend from below the bend, it induced a bifurcation of flow in the bend causing the plume to fold onto itself.

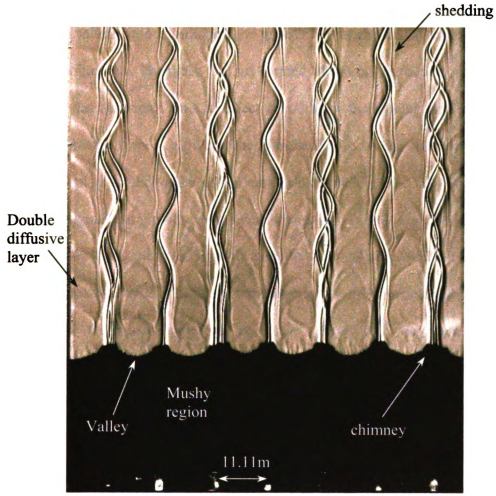


Figure 3.1.4. Image of solidification process at 2 hours.

As the plumes rise above the chimney, at about 10mm away, the plumes start to take on a three-dimensional helical motion, which has been reported by many researchers (Stuebe and Hellawell, 1992; Magirl and Incropera, 1993). When the plumes begin to oscillate, wisps of fluid separate from the plume and descend as shown. Significant shedding can be seen at the plume edges as it makes the turn, with the shedding becoming more pronounced as the solidification continues. Figure 3.1.4 shows a few important features present in the flow. (Note: There are two plumes, overlapping each other starting on the far left and alternates to the far right due to the nucleator positions, see Figure 2.1.2 for nucleator positions)

As the solidification continues, the growth rate of the mushy zone decreases due to a slower cooling rate. The mush that has formed acts as an insulated boundary between the fluid and the base plate thus in effect shielding it from being cooled further. The height of the mushy zone at a given time is measured to be the distance from the base stainless steel plate to the valley of the mush as shown Figure 3.1.4. From the plot in Figure 3.1.5, significant growth of the mush occurs in the early stages of the experiment from ~5 minutes to 40 minutes before it starts to taper off and level out at a maximum height of approximately 27mm. Two separate trials were conducted showing that the growth rate of the mushy zone was consistent. Magirl and Incropera's experiments utilized a cooling temperature of $-30^0$C, which resulted in an earlier formation of the fingers as compared to the present study, which cooled the base plate to a minimum temperature of $-14^0$C.

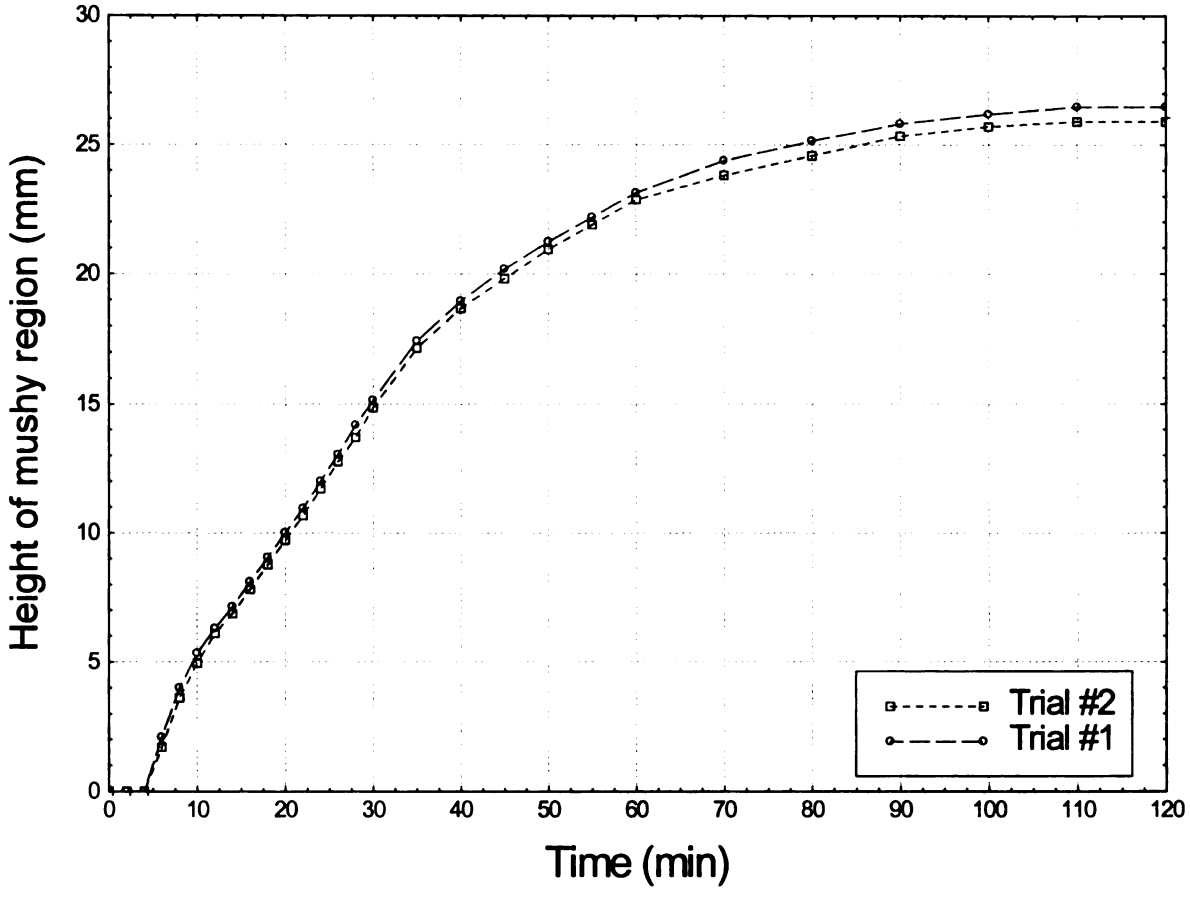


Figure 3.1.5. Plot of Height of Mushy Region vs. Time

### 3.2 MTV Measurements of Mushy Region

One of the features in the solidification process that is of interest is the small fingers present at the onset of the solidification process. The MTV measurements of these water-rich fingers yield quantitative information describing the velocity field just above the mushy zone. Velocity measurements were made in these regions at various times to better understand the permeability of the mush. During the experiment, a total of 60 images were taken at each time tick, of which 15 pair of images would contain the image of the tagged field of view. This yields 15 velocity realizations over a 2-second period. For the first field of view, measurements were made from 0 minutes to 40 minutes before the mushy region covered the field of view completely. At about 20 minutes, the mushy zone would have grown to the base of the laser line tagging and would continue to grow until the entire field of view was covered. Figure 3.2.1 shows the tagging region with respect to the solidification process at 8 minutes.

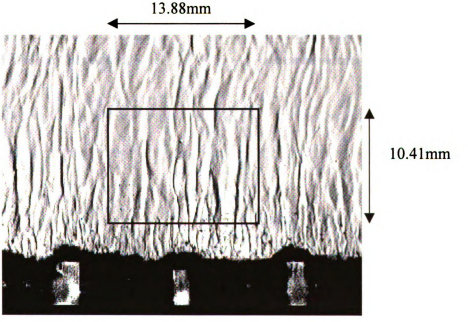


Figure 3.2.1. Tagging region of the 1st FOV at 8 minutes into the solidification process

Figure 3.2.2 and Figure 3.2.3 illustrate the instantaneous realizations of the velocity fields obtained from an MTV measurement of the region above the mushy layer for the first field of view where the bottom is 10.5mm from the base stainless steel plate. The y-axis indicates the location of the field of view with respect to the base stainless steel plate. In Figure 3.2.2, the velocity vectors displayed at 4 minutes is an instantaneous realization due to significant variation between the 15 realizations. All other velocity vectors are averaged over 15 realizations to reduce the amount of noise.

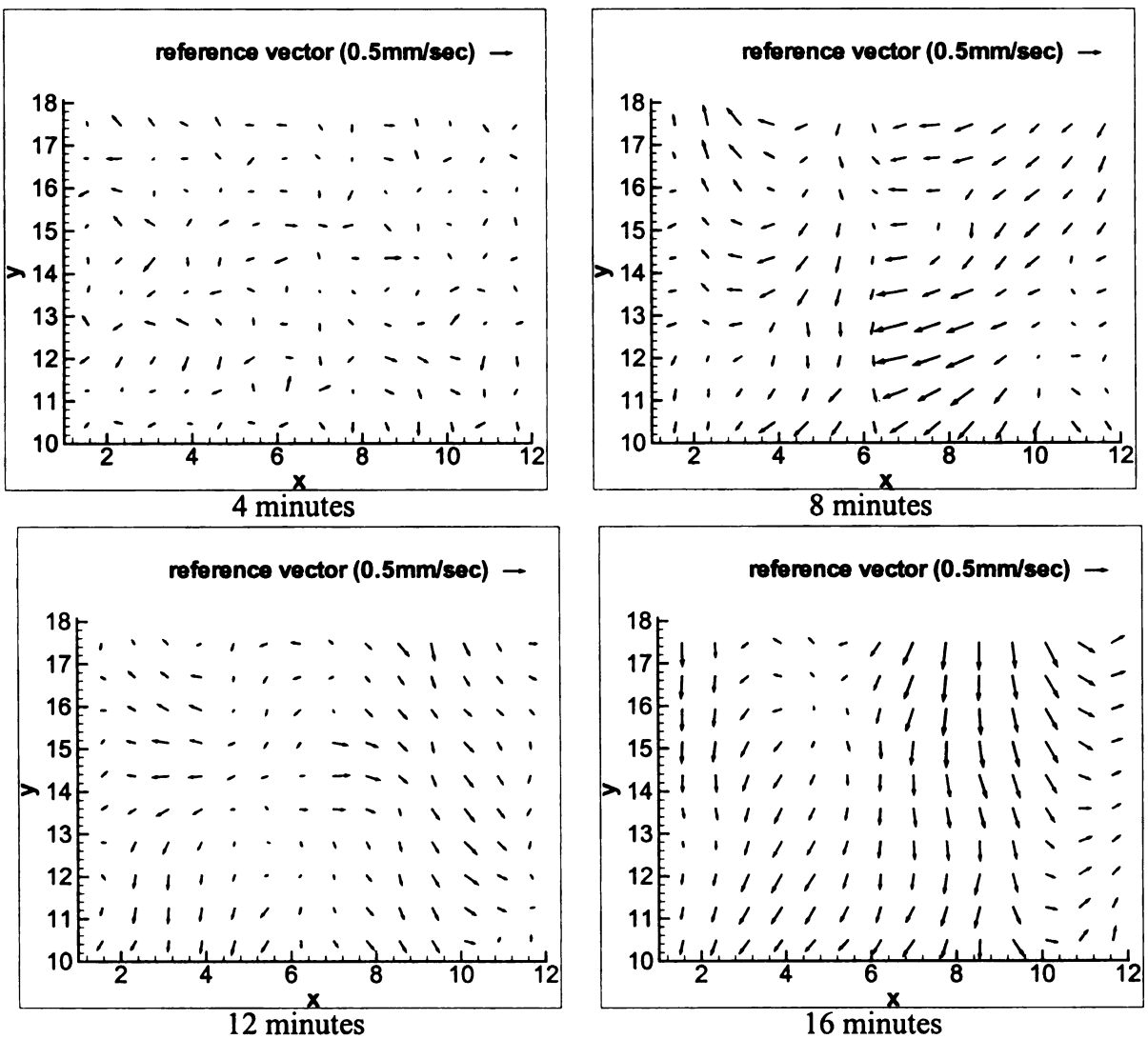


Figure 3.2.2. Velocity fields of mushy region at 4 minutes (instantaneous) and from 8-16 minutes (averaged) in the 1st FOV

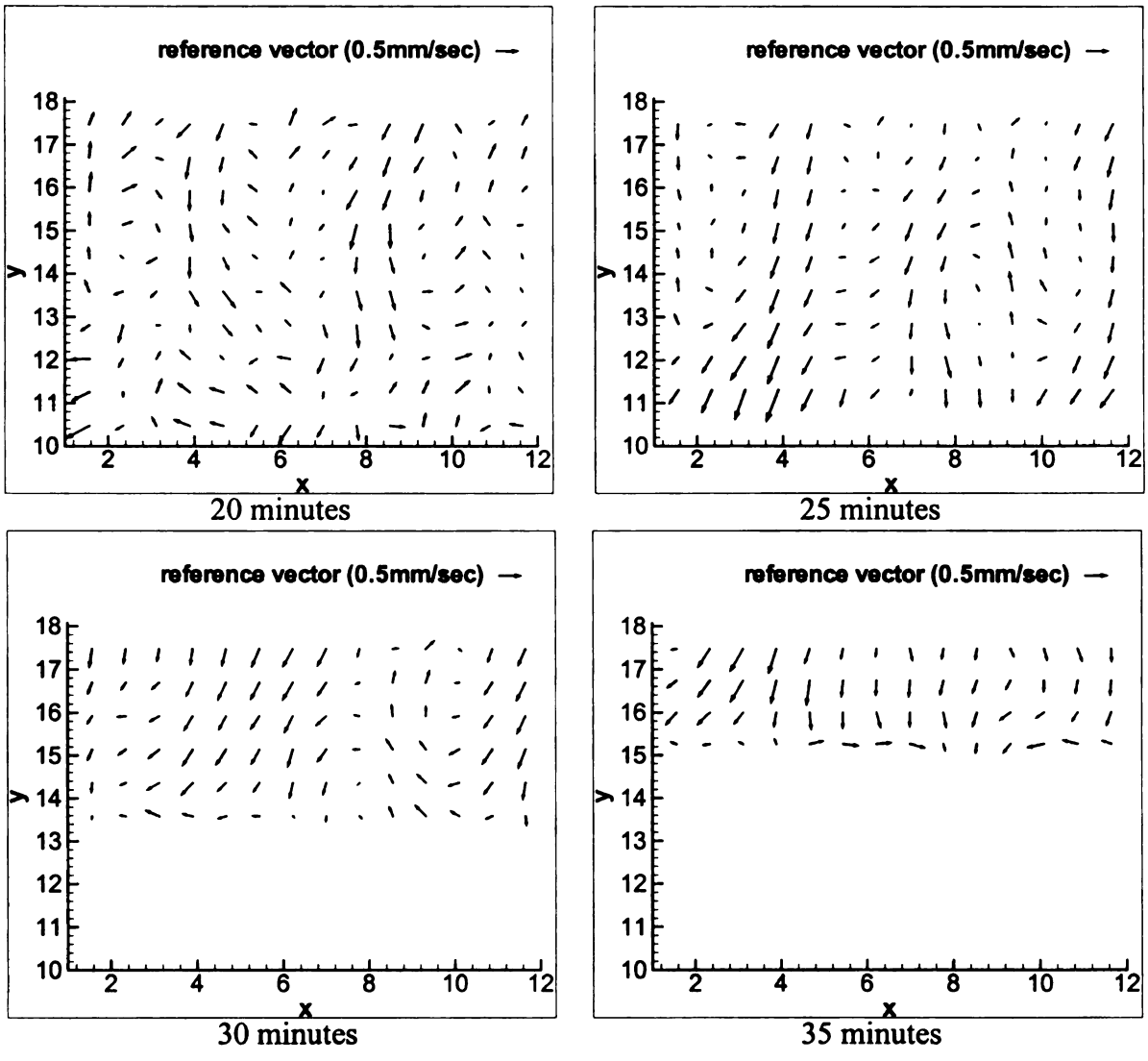


Figure 3.2.3. Averaged velocity fields of mushy region from 20-35 minutes (1st FOV)

Even at an early stage in the experiment, a well-defined convective flow has already formed. However, the velocities were not solely in the upward direction, which was originally thought, as depicted by the *u* component of the velocity (note: *u* component of velocity is in the x direction), which has the same order of magnitude as the *v* component of velocity. It is apparent from the measurements that the velocities of the small fingers are on the order of 1mm/s and the velocity components in both the x and y directions are comparable. Note that for measurements on this order of magnitude, the

maximum displacement of the laser grid is about 4 pixels in the field of view of 10.41 x 13.88 mm which translates to a velocity of 1.6 mm/s with a delay time between the delayed and undelayed images to be 56.995ms. The maximum velocities are documented in Table 1 on page 47.

By looking at Figure 3.2.2, at 8 minutes, it can be seen that well-defined convective flow patterns have formed at this early stage in the experiment. At 16 minutes, the flow is generally in the downward direction with slight movement of the fluid in the upward direction at the far right of the field of view while at 20 minutes, the flow pattern seems to return to the initial chaotic pattern that was exhibited at 4 minutes, albeit with a higher magnitude of velocity. One feature that is of interest is shown at 35 minutes where the velocity vectors at the very bottom of the field of view seem to congregate to one location. Salt-rich fluid descends to fill the void left by the ascending fingers. This salt-rich fluid would approach the mush and due to the undercooling that the fluid experiences, precipitates ammonium chloride and finally ascends as water-rich fingers. This process continues as the mushy region grows in height.

In the second data set, the same image ratio was used but at a height of 21mm from the base stainless steel plate. Figure 3.2.4 shows the location of the tagging region for the 2$^{nd}$ FOV relative to the solidification process at 8 minutes. The second field of view acts to document the velocities above the mushy zone after 40 minutes when the first field of view is completely blocked and also at earlier times to observe the fluid movement at a farther distance from the mushy region. The following figures illustrate the measured velocity vectors at different times into the solidification process. All the velocity vectors shown are averaged over 15 realizations in a time frame of 2 seconds.

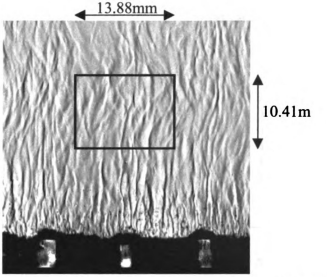


Figure 3.2.4. Tagging region of the 2nd FOV at 8 minutes into the solidification process

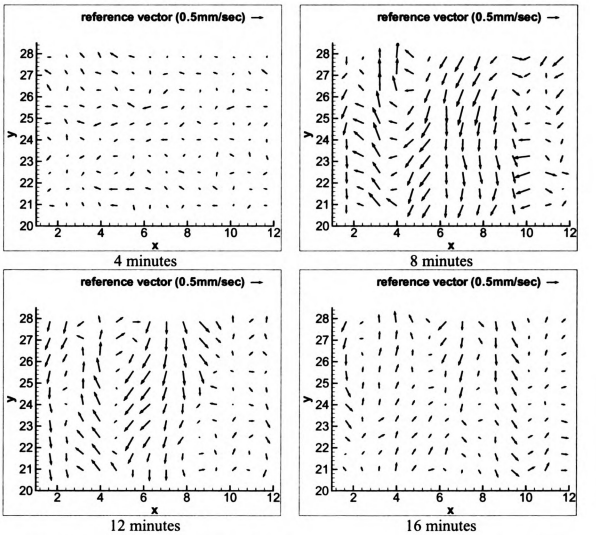


Figure 3.2.5. Averaged velocity fields of mushy region from 4-16 minutes (2nd FOV)

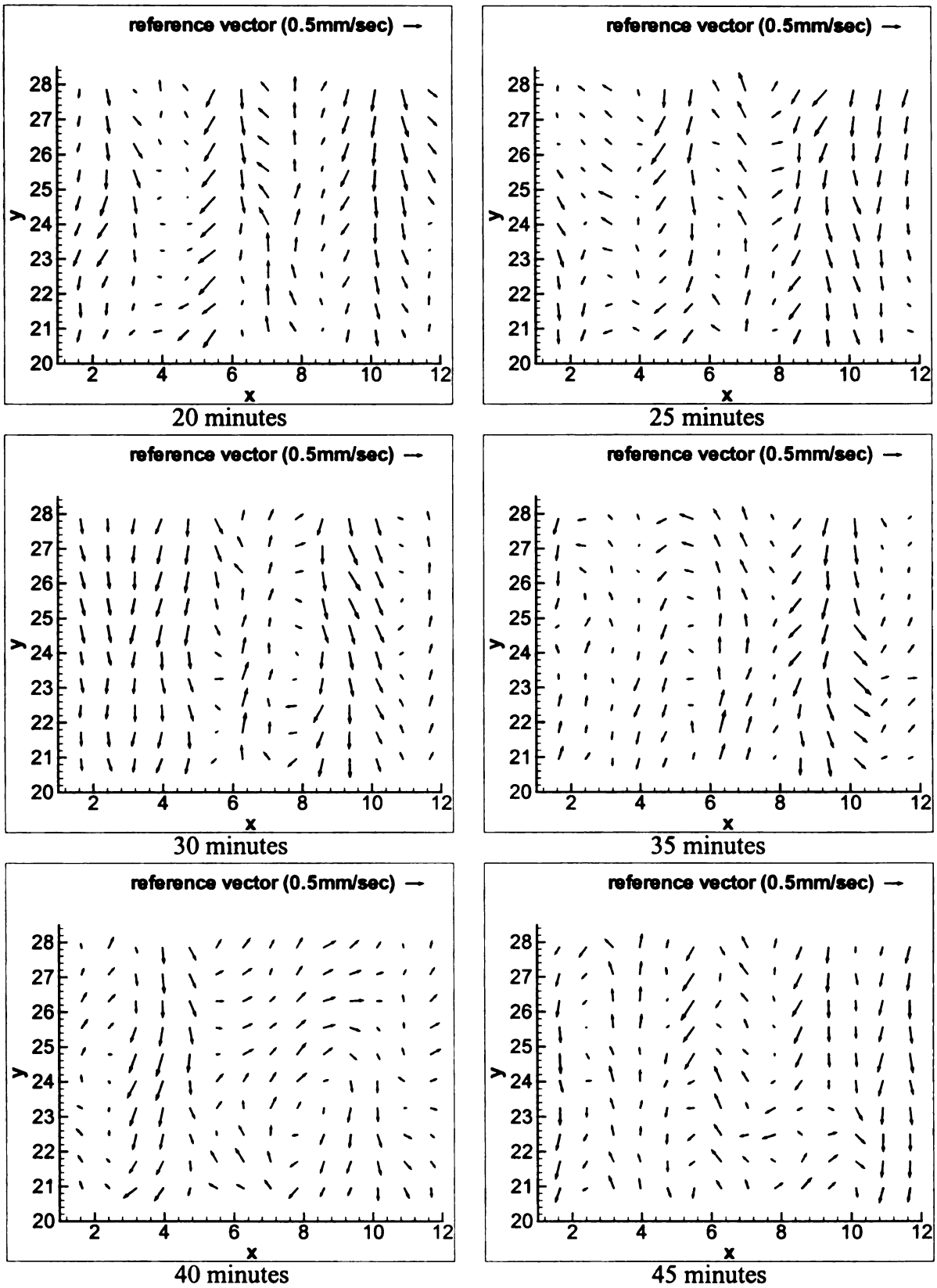


Figure 3.2.6. Averaged velocity fields of mushy region from 20-45 minutes(2nd FOV)

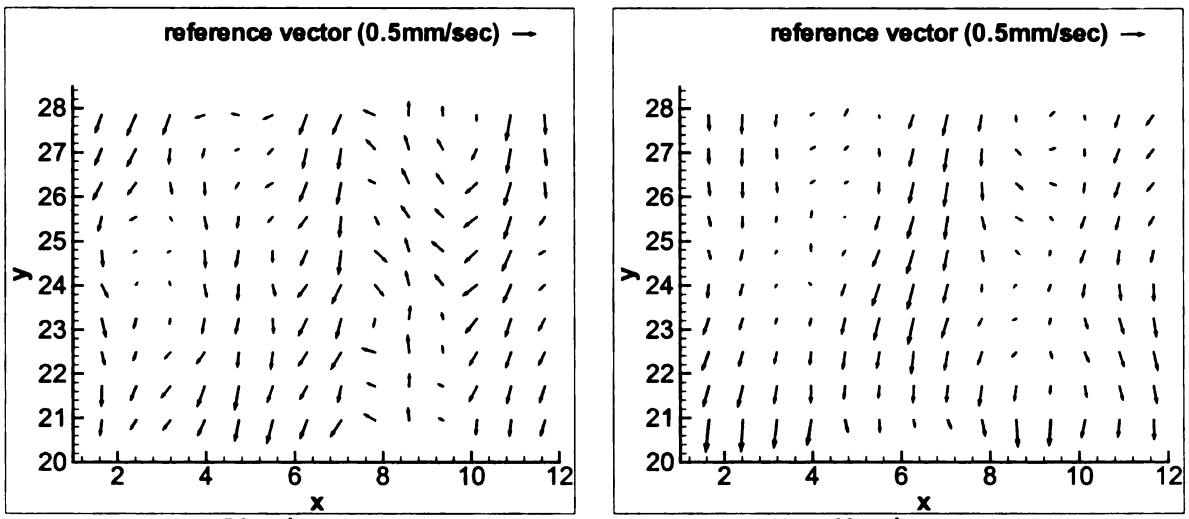


Figure 3.2.7. Averaged velocity fields of mushy region from 50-60 minutes(2nd FOV)

From Figure 3.2.5, it can be observed that at 8 minutes into the solidification, an obvious downflow is occurring in the middle of the field of view coupled by a slight rise of the fluid on the left side. This is typical of the fluid flow phenomena at this stage of the experiment where lighter fluid rise as water-rich fingers and salt-rich fluid descends to fill the void present. All the instantaneous realizations of the velocity measurements made in the FOV showed a well-defined convective flow pattern with velocities on the order of 1mm/sec, similar to velocity measurements made in the 1st FOV. At around 65 minutes into the solidification process, the mushy region would have covered part of the field of view. A third field of view was taken to measure the fluid velocity at a time later than 65 minutes. The 3rd FOV is located at 31.5 mm from the base stainless steel plate while the maximum height of the mushy zone is only ~27mm. Thus the laser-tagging pattern would not be obstructed by the mushy region in this field of view. Figure 3.2.8 shows the relative location of the tagging region with respect to the solidification process at 8 minutes.

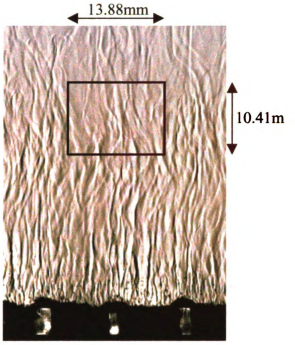


Figure 3.2.8. Tagging region of the 1st FOV at 8 minutes into the solidification process

Figures 3.2.9, 3.2.10 and 3.2.11 illustrate the velocity field measurements made in this field of view.

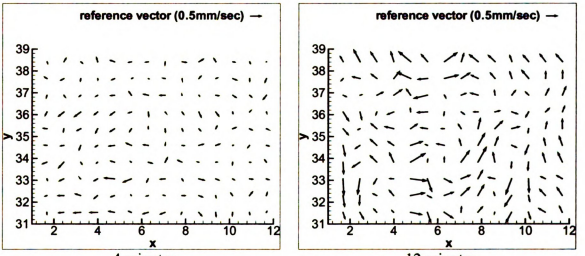


Figure 3.2.9. Averaged velocity fields of mushy region at 4 and 12 minutes (3rd FOV)

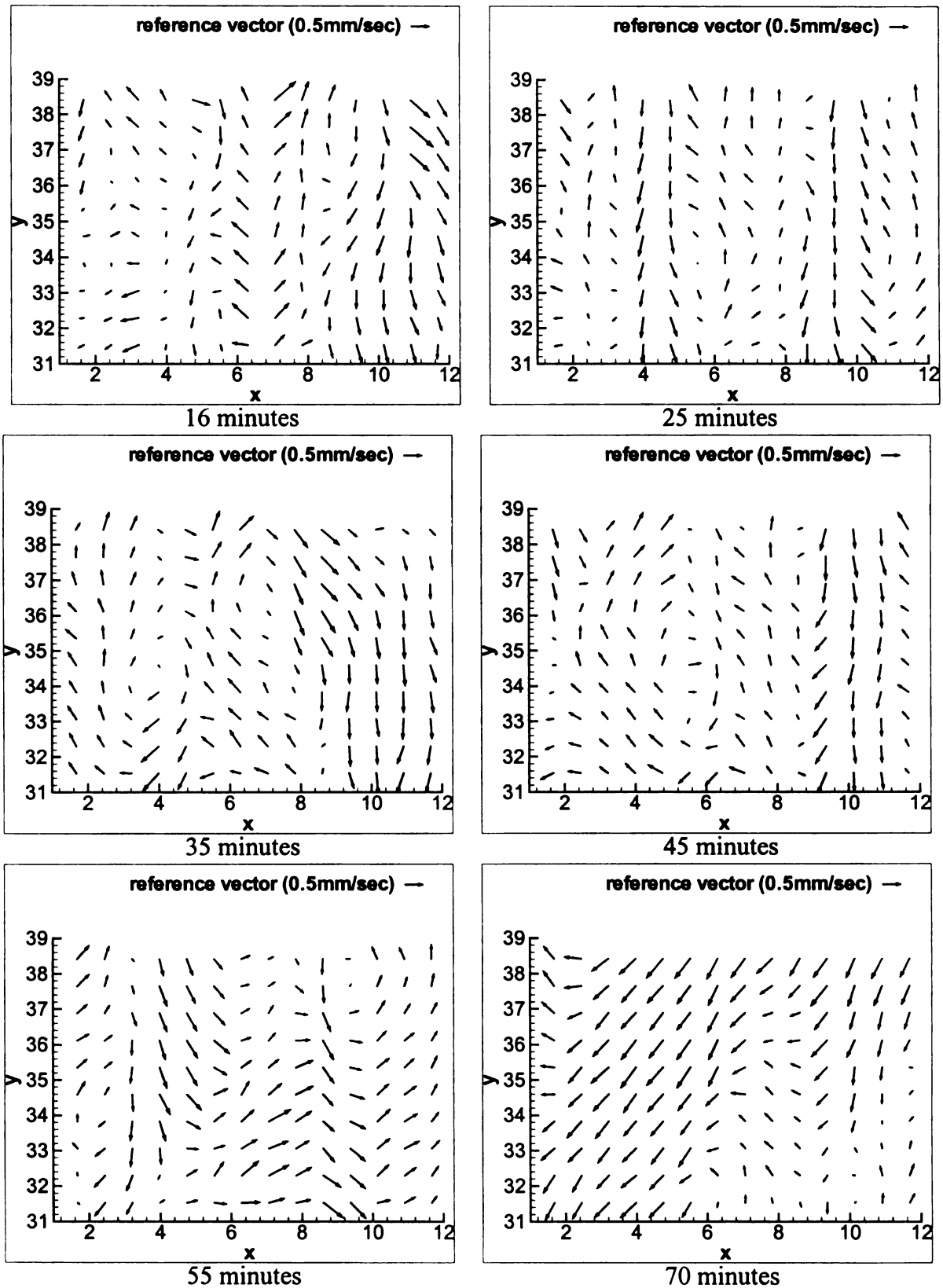


Figure 3.2.10 Averaged velocity fields of mushy region from 16-70 minutes(3rdFOV)

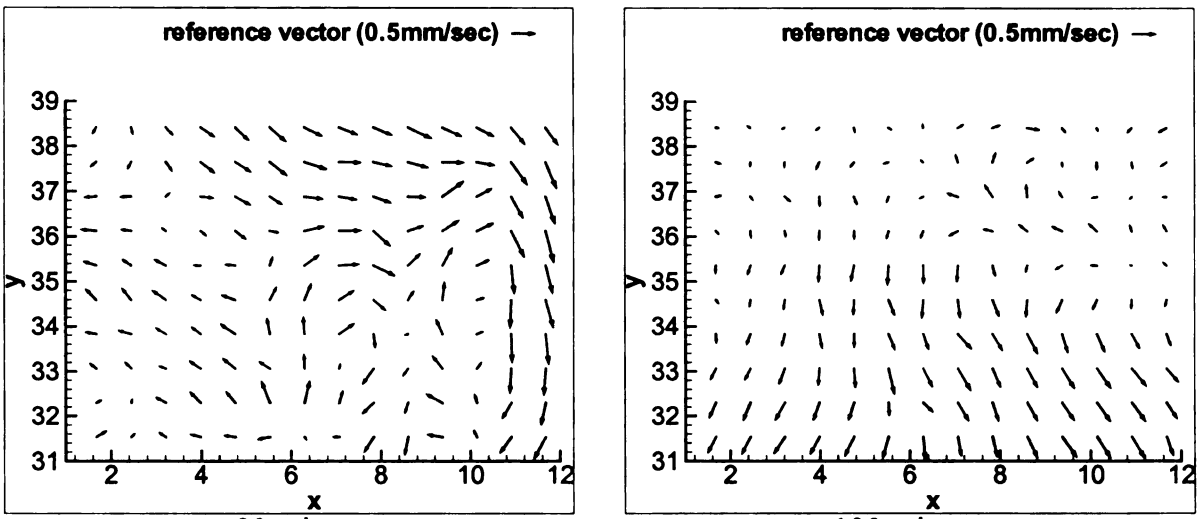


Figure 3.2.11. Averaged velocity fields of mushy region at 80, 100 minutes (3rd FOV)

Tables 1, 2 and 3 condense the respective maximum or minimum U and V component velocities present in the three fields of view. In all three fields of view, the velocity field is seen to have a velocity magnitude in the U and V component of order 1mm/sec. In the first field of view, the maximum velocity magnitude in the V component generally occurs in the downward direction.

| Time (minutes) | U - Component (mm/sec) | V - Component (mm/sec) |
|---|---|---|
| 8 | -0.76 | -0.43 |
| 12 | 0.44 | -0.43 |
| 16 | 0.46 | -0.60 |
| 20 | -0.42 | -0.48 |
| 25 | -0.32 | -0.54 |
| 30 | -0.24 | -0.47 |
| 35 | -0.38 | -0.58 |
| 40 | -0.24 | -0.39 |

Table 1. Instantaneous maximum/minimum velocity measurements in the 1st FOV near the mushy zone.

| Time (minutes) | U - Component (mm/sec) | V - Component (mm/sec) |
|---|---|---|
| 8 | -0.39 | 0.61 |
| 12 | -0.43 | 0.73 |
| 16 | -0.35 | 0.61 |
| 20 | -0.35 | 0.61 |
| 25 | -0.42 | 0.67 |
| 30 | -0.31 | -0.70 |
| 35 | -0.47 | -0.70 |
| 40 | -0.34 | -0.52 |
| 45 | -0.32 | -0.53 |
| 50 | -0.36 | -0.44 |
| 55 | -0.36 | -0.70 |
| 60 | -0.30 | -0.53 |

Table 2. Instantaneous maximum/minimum velocity measurements in the 2nd FOV near the mushy zone.

| Time (minutes) | U - Component (mm/sec) | V - Component (mm/sec) |
|---|---|---|
| 12 | 0.60 | 0.79 |
| 16 | 0.52 | 0.58 |
| 20 | 1.03 | -0.67 |
| 25 | -0.66 | 0.64 |
| 30 | 0.49 | -0.82 |
| 35 | 0.33 | -0.58 |
| 40 | 0.62 | -0.63 |
| 45 | 0.32 | -0.66 |
| 50 | 0.65 | -0.86 |
| 55 | 0.43 | -0.59 |
| 60 | 0.64 | -0.53 |
| 70 | -0.47 | -0.60 |
| 80 | 0.59 | -0.74 |
| 90 | 0.47 | -0.32 |
| 100 | 0.34 | -0.44 |
| 110 | 0.41 | -0.44 |
| 120 | -0.43 | -0.45 |

Table 3. Instantaneous maximum/minimum velocity measurements in the 3rd FOV near the mushy zone.

### 3.3 MTV Measurements above Chimney

In the regions above the chimney, previous research obtained a peak velocity in the vicinity of 8mm/s. Figures 3.3.1 and 3.3.2 illustrate the velocity profile and the delayed image using single line tagging just above the chimney. (Wirtz et. al., 1998)

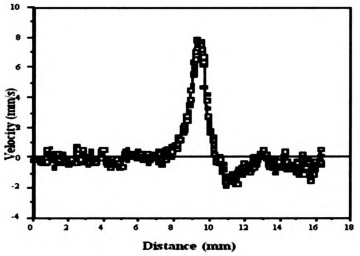


Figure 3.3.1. Velocity profile of plume (Wirtz et. al., 1998)

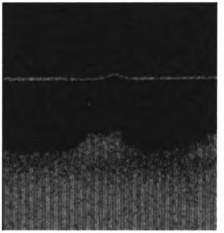

Figure 3.3.2. Delayed image using single line tagging (Wirtz et. al., 1998)

The measurements of the velocity field of the plume in this study are divided into two parts. In regions near the chimney, two component measurements of the velocity were not performed due to the way the experimental setup was configured. As shown in Figure

2.1.1, the nearest the two-component measurement technique can get to the mushy region is 7mm. In order for velocity measurements at distances lower than this, single laser lines were passed through the field of views similar to the ones used for measurements just above the mushy region. It should be clarified that the chimney itself is part of the mushy region but measurements of the mushy region apply only to locations where plumes do not exist while all plume measurements relate to the location above the chimney.

In the single component velocity measurements, it is assumed that the main velocity component is in the upward (V) component. This however is not entirely true but the U component is assumed to be negligibly small thus allowing us to validate the assumption of single component velocity very near the chimney. Figure 3.3.3 illustrates the region where single line tagging was performed.

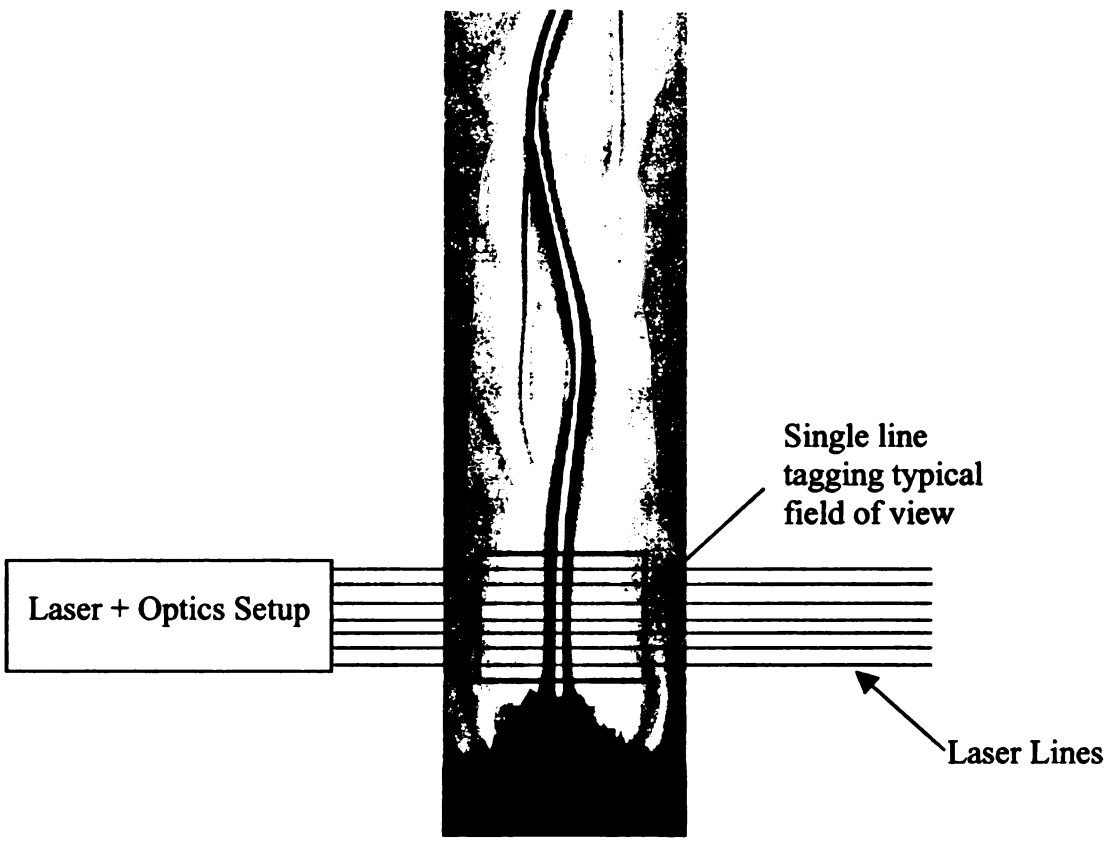


Figure 3.3.3. Typical location of multiple line tagging of single component measurements

The single velocity component measurements were performed in a field of view with the lowest laser line being 21.0mm away from the base stainless steel plate. Typically, 12 laser lines are used in a single field of view. The velocity measurements are illustrated in the following figures.

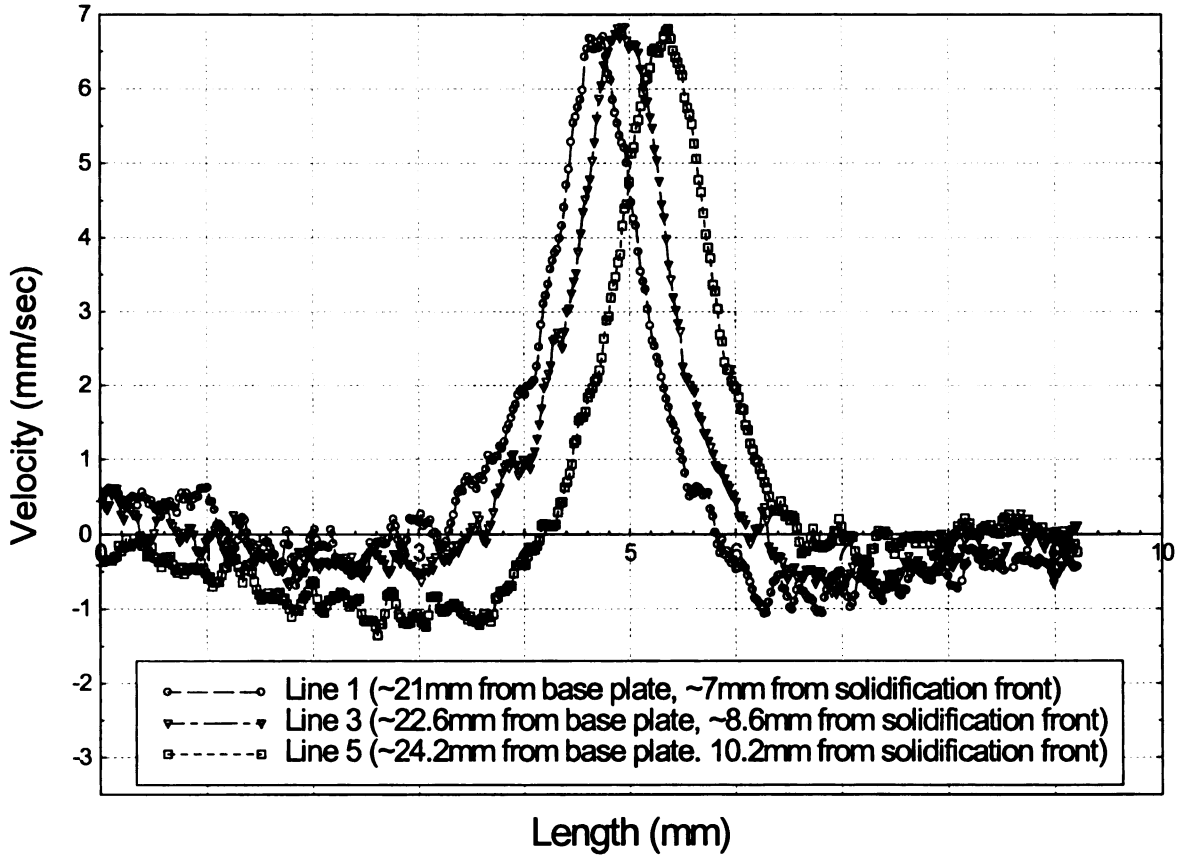


Figure 3.3.4. Single component velocity measurement of plume at 28 minutes

In Figure 3.3.4, the velocity measurements showed that at three locations above the chimney, the plume exhibited a velocity component of ~ 7mm/s. This is in agreement with the results obtained by Wirtz et. al (1998) which exhibited a velocity component of ~8mm/s. Magirl and Incropera (1993), reported velocity measurements of ~10mm/s due to their much lower cooling temperature of -30°C which resulted in a higher rate of

cooling and growth of the mushy region. This contributed to the need for a higher flow for rejection of water-rich fluid from within the mushy region.

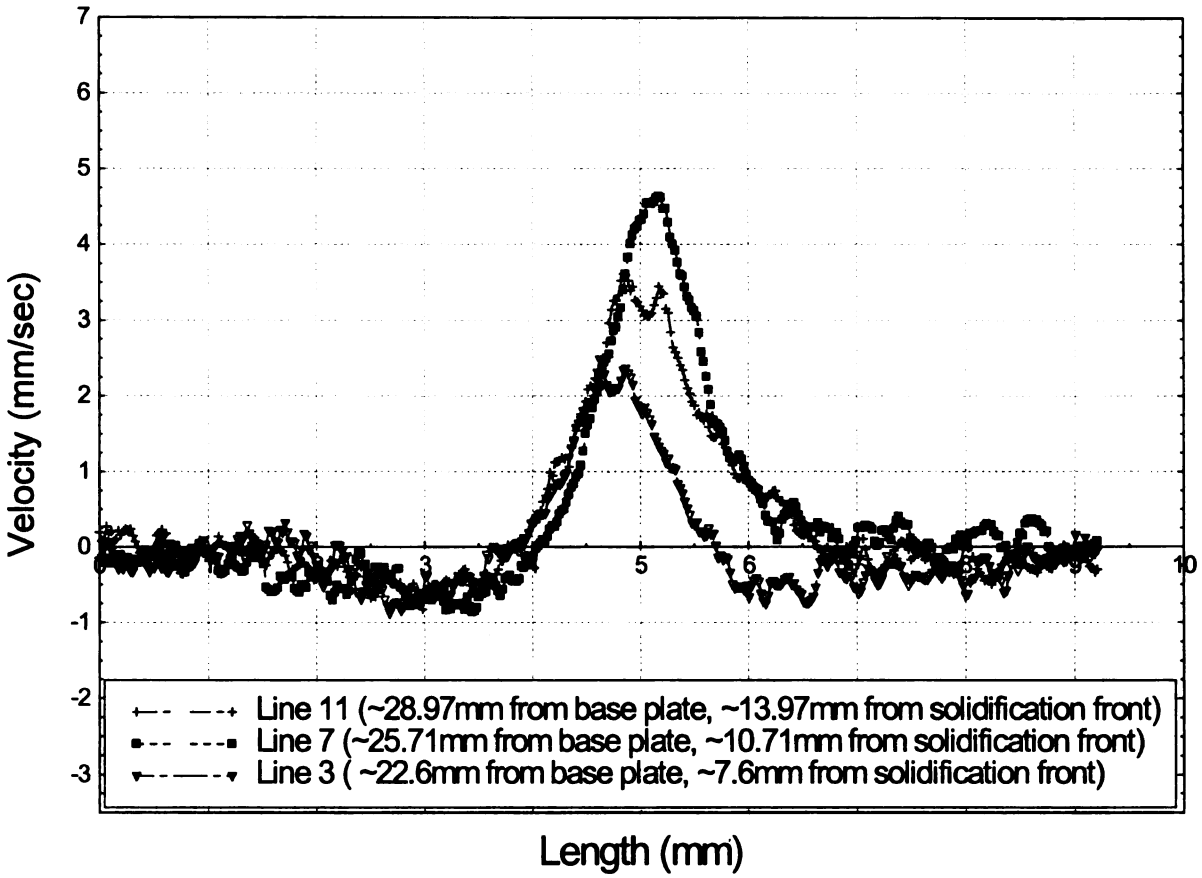


Figure 3.3.5. Single component velocity measurement of plume at 30 minutes

In Figure 3.3.5, the velocity measurements are noticeably lower than in Figure 3.3.4. The maximum velocity in Figure 3.3.5 is less than 5mm/sec. However, one noticeable phenomenon in both Figures 3.3.4 and 3.3.5 is the lateral displacement of the tagging lines at different vertical locations. This indicates that the plume has a lateral component of velocity, which was not taken into account during the correlation of the velocity. The correlation technique used assumes a pure $v$ component of velocity. Thus there is an inherent error in the correlation technique used in the single line tagging which would tend to compute a lower velocity. However it provides a good estimate of the velocity

component. Another feature of interest in the velocity measurements as shown in Figure 3.3.5 is the double peak present on line 3 and 11. This feature has been repeatedly observed especially in regions of lower speeds. As the plume traverses the plane of illumination, the velocities can be seen to increase from line 3 to line 7 and decrease again on line 11. Due to the planar nature of the tagging method, all velocity measurements can only be made over a plane. Whenever the plume moves out of plane, the laser lines would be tagging the edge of the plume and not inside it, which may result in lower velocity measurements. Figures 3.3.6, 3.37 and 3.38 illustrate measurements made at different times within the field of view that was used in the one-component velocity measurement with line tagging. Uncertainty calculations are under progress.

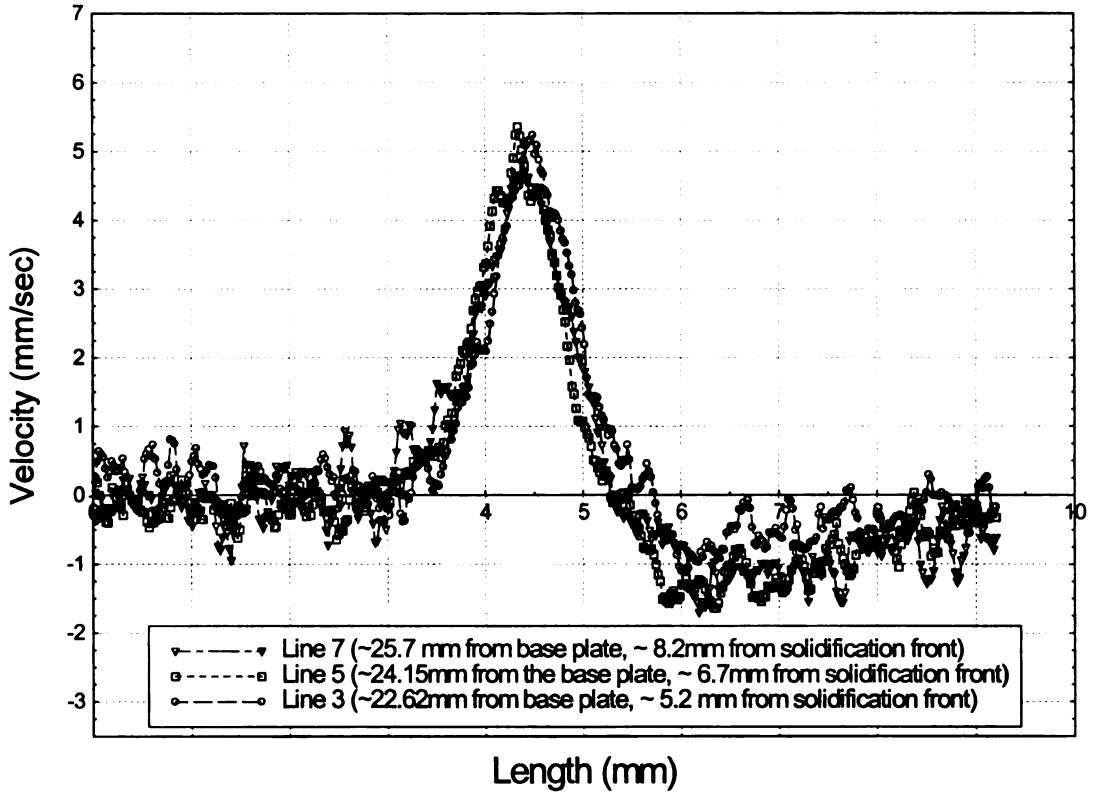


Figure 3.3.6. Velocity profile of plume at 35 minutes into the solidification process

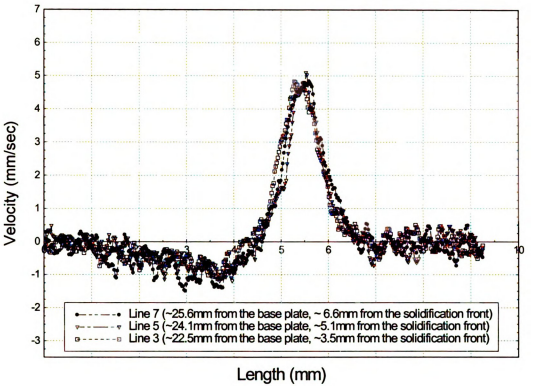


Figure 3.3.7. Velocity profile of plume at 40 minutes into the solidification process

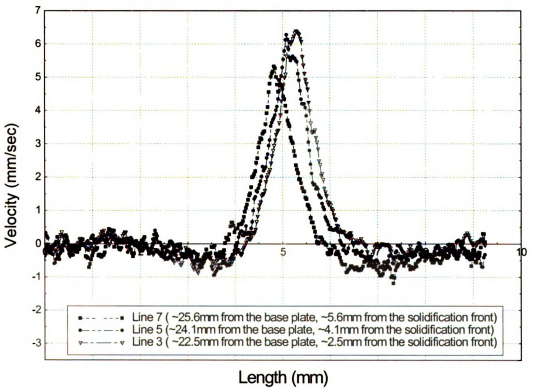


Figure 3.3.8. Velocity profile at 45 minutes into the solidification process

At a larger distance away from the chimney, two-component velocity measurements were implemented. The tagging pattern for measurements of the plume is rotated by ~45 degrees compared to the tagging pattern of the mushy region. This is due to problems encountered with the index of refraction of the plume when vertical laser lines intersect the edge of the plumes as shown in Figure 2.2.5. From the two-component velocity measurements obtained above the chimney, it can be seen that the flow is generally moving in the upwards direction with velocities of order 6.5mm/s. The U-component velocities are seen to be typically less than 2mm/s. Figure 3.3.9 illustrates the location of the plume with respect to the fields of view at $t_o$=79 minutes into the solidification process. The bottom of the field of view is 35mm from the base plate.

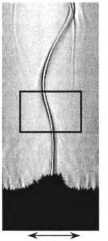


Figure 3.3.9. Visualization of tagging region at 79 minutes into the solidification process

In Figure 3.3.9, in the tagging region of 10.41mm *x* 13.88mm, by observing a sequence of images, fluid can be seen descending on the upper right corner from shedding that occurred at a distance above the field of view while slight shedding can be seen on the left edge of the plume. This phenomenon is captured in the velocity measurements and shown in Figure 3.3.10.

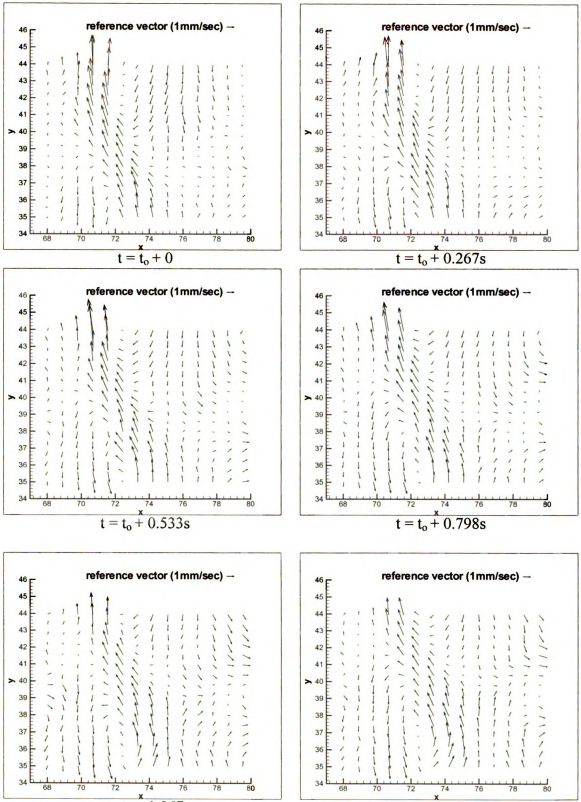


Figure 3.3.10. Velocity vectors measured at $t_o$ = 79 min of plume from $t_o$ to $t_o$ + 1.33s

From Figure 3.3.10, at $t_o = 0$, the maximum velocity within the field of view occurs at the very top of the measurement grid. The velocity vector translates to a velocity of ~4mm/s in the upward component. However, this may not be the maximum velocity within the plume itself as the laser tagging plane may not be entirely coincident with the plume. As we observe the sequence of images from $t = t_o$ to $t = t_o + 1.333$s, the plume is slightly swinging to the right of the field of view as it rejects fluid in the upward direction. In the process, fluid in the upper right corner descends which may be caused by shedding at a higher location as shown in Figure 3.3.10 and some gets entrained within the plume. Some downward movement of the fluid can also be seen on the lower left corner of the fields of view as some shedding of the fluid occurs as the plume tries to traverse a bend. The velocities measured in this region are typically less than 1mm/s.

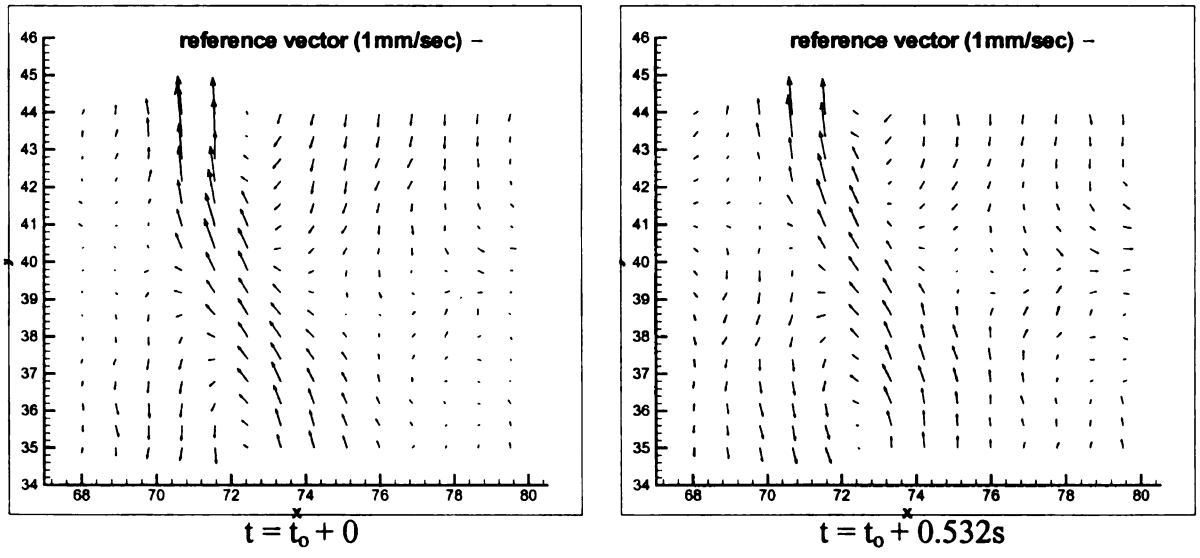


Figure 3.3.11. Velocity measurements at $t_o = 75$ minutes into the solidification process

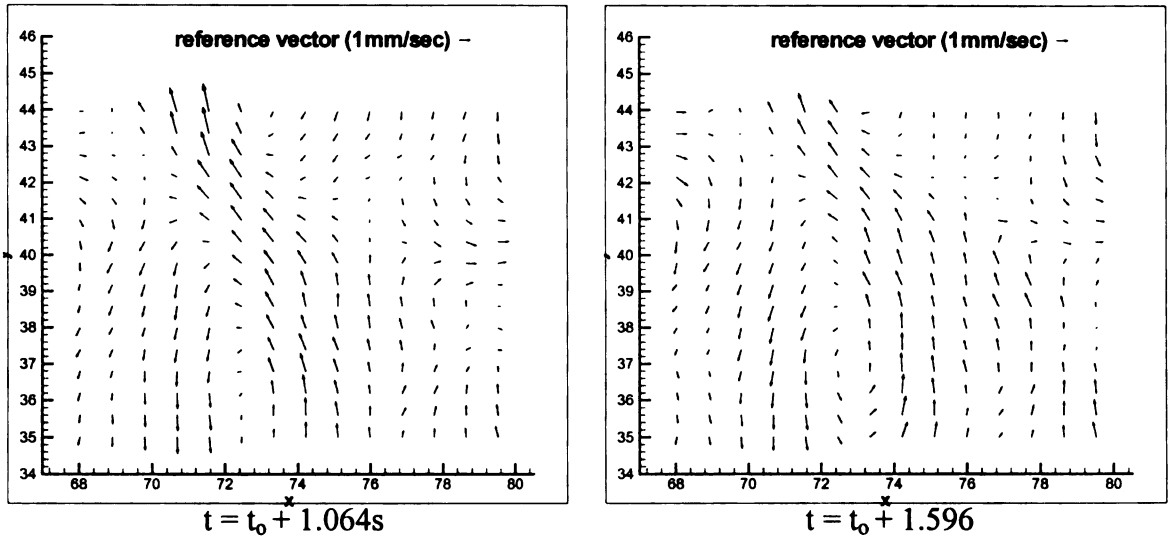


Figure 3.3.11. Velocity measurements at $t_o$ = 75 minutes (continued)

As the movement of the plume becomes helical, tagging the plume becomes difficult as the plume moves in and out of the tagging plane. In the image sequence taken at a specific time, it is often observed that the plume is tagged at an earlier time tick but slowly moves out of the tagging plane later in time. This makes it more difficult to determine the velocity of the plume itself. In Figure 3.3.11, an example of this difficulty is illustrated in the velocity measurements.

This difficulty in tagging the plume is particularly apparent as the solidification process continues and the plume becomes more three dimensional in nature. The measurement technique employed in this study can only measure the in-plane velocity fields. Any out of plane velocity field can only be measured with a stereoscopic implementation of MTV. The following figures are velocity measurements at different times within the same field of view. All the figures are instantaneous realizations and are not representative of the 15 realizations taken at each time tick. As the flow field changes dramatically within the time frame of 2 seconds, an average velocity vector would not yield any useful information.

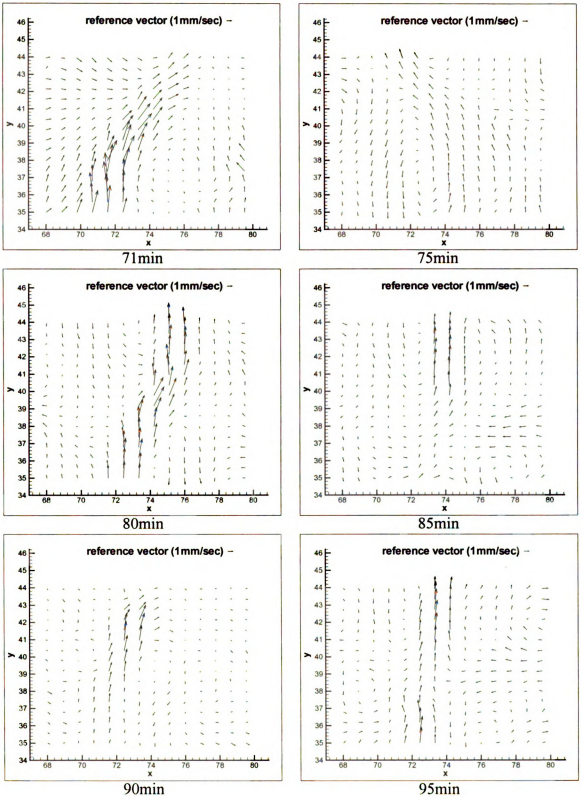


Figure 3.3.12. Instantaneous velocity measurements of plume from 71 to 95 minutes.

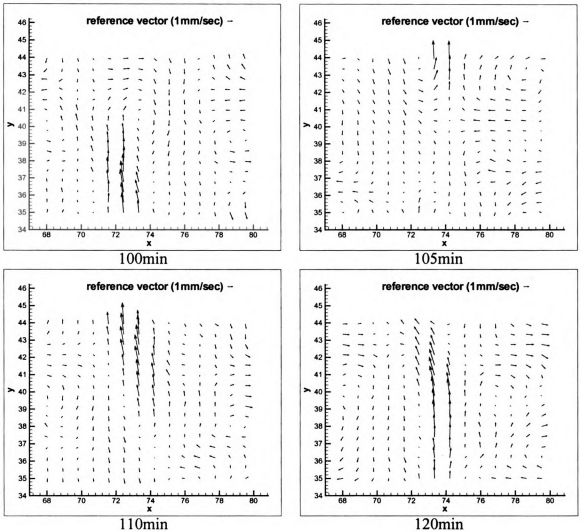


Figure 3.3.13. Instantaneous velocity measurements of plume from 100 to 120 minutes.

Many convective features that were apparent in the flow visualization were measured by the MTV technique. At 71 minutes into the solidification process, it can be seen that the plume has a velocity of ~7mm/s with surrounding fluid moving at a velocity of ~ 1mm/s. Plume shedding was also measured with velocities on the order of 1mm/s. Table 4 condenses the maximum or minimum velocity components of measurements made.

| Time (minutes) | U - Component (mm/sec) | V - Component (mm/sec) |
|---|---|---|
| 71 | 1.77 | 6.49 |
| 75 | -0.97 | 4.98 |
| 76 | -0.97 | 4.98 |
| 77 | -1.66 | 4.75 |
| 78 | -0.89 | 4.03 |
| 79 | -0.88 | 5.40 |
| 80 | 1.17 | 4.40 |
| 81 | 1.30 | 3.19 |
| 82 | -1.10 | 3.18 |
| 83 | 1.20 | 1.77 |
| 84 | 1.72 | 4.44 |
| 85 | -1.33 | 4.18 |
| 86 | 1.87 | 4.88 |
| 87.5 | 1.28 | 4.53 |
| 88 | 1.03 | 4.24 |
| 90 | 1.10 | 2.70 |
| 91 | 1.08 | 5.25 |
| 92 | -1.00 | 3.02 |
| 93 | -1.49 | 4.28 |
| 94 | -1.11 | 4.28 |
| 95 | -1.32 | 3.76 |
| 96 | 1.44 | 4.14 |
| 97 | 0.74 | 3.96 |
| 99 | -0.59 | 3.69 |
| 100 | -0.59 | 4.71 |
| 101 | 1.46 | 4.49 |
| 105 | -1.39 | 3.65 |
| 110 | 0.70 | 3.39 |
| 120 | 1.41 | 3.83 |

Table 4. Instantaneous maximum/minimum velocity measurements for the plume

### 3.4 Flow Rate Calculation above the Mush

In trying to determine the porosity of the region just above the mush, the average speed was computed for all y locations for select time ticks of the three fields of view of measurements of the mushy region. The V-component of velocity is integrated over the entire constant y location to obtain an average speed moving across the particular y location. This procedure is performed at multiple locations and time ticks to produce contour plots. The equation utilized for the calculation of the average speed is as shown below:

$$\frac{\int\int V \cdot dxdz}{\Delta x}$$

Since velocity information is not available in the z plane, we assume the *dz* term to be unity. By dividing the integrated value of velocity, V, by $\Delta x$, we essentially obtain an average speed in mm/s.

The following figures show the contour plots that were obtained from the calculation of the average speed above the mush at the three fields of view.

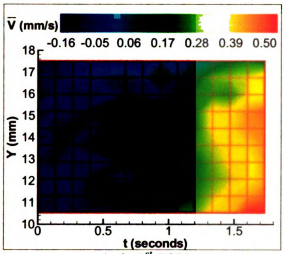


4min 1st FOV

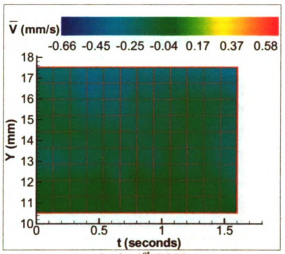


8min 1st FOV

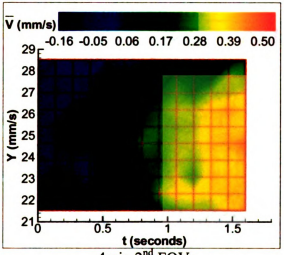


4min 2nd FOV

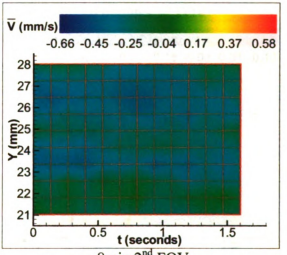


8min 2nd FOV

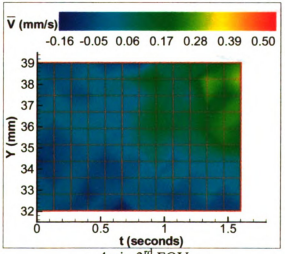


4min 3rd FOV

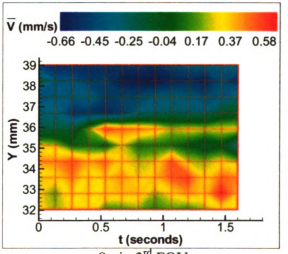


8min 3rd FOV

Figure 3.3.14. Flow rate plots at 4 and 8 minutes of three field of views.

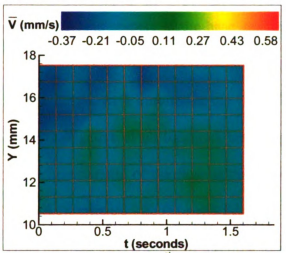


12 minutes 1st FOV

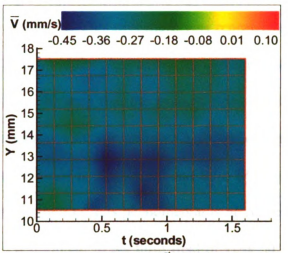


16 minutes 1st FOV

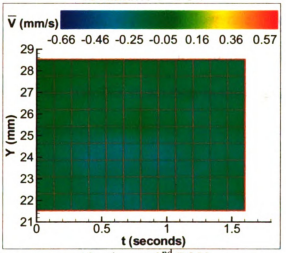


12 minutes 2nd FOV

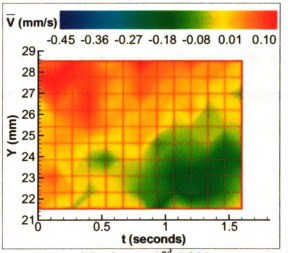


16 minutes 2nd FOV

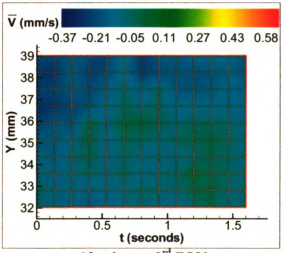


12 minutes 3rd FOV

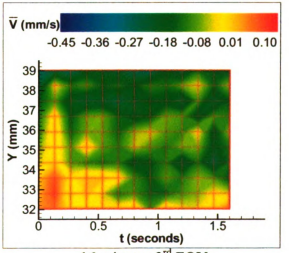


16 minutes 3rd FOV

Figure 3.3.15. Flow rate plots at 12 and 16 minutes for three field of views.

In Figures 3.3.14 and 3.3.15, Y designates the location where the speed was computed with respect to the base stainless steel plate. This procedure was repeated at different Y locations and at different time ticks to yield the plots above for average flow rate in mm/s. At 4 minutes in the 1st FOV, it can be seen that the average flow rate is initially negative at all locations before becoming positive at around 1.5 seconds later. This characteristic of the flow at this time is exhibited in the second and third FOV as well. At 8 minutes into the solidification process however, this phenomenon is no longer observed and the variation of the flow in time is minimal. In the third field of view, at a lower location, a positive flow rate is evident while a negative flow rate seems to dominate at a higher location. At 12 minutes and 16 minutes, flow variations in time are also minimal. The fluctuation in the magnitude of the flow rate is observed to be highest at 8 minutes.

# Chapter 4: Conclusion

In this study, the uni-directional solidification of a binary alloy was studied. The test facility used in conducting the experiments is the same as that utilized by Kay Wirtz at Michigan State University (Wirtz, et. al. 1998) with some modifications added to allow the full two-component implementation of the MTV technique. However, this setup proved to be inadequate due to the amount of condensation that forms on the outer quartz walls whenever an experiment was performed. This is detriment to the penetration of the laser lines used for tagging purposes during the summer season as the humidity of the ambient air increases substantially. It is also observed that the solidification process is affected by the air temperature, especially the height of the mushy region, which peaked during the winter months. To ensure that the different measurements were essentially measuring the same process, the entire data set needs to be coordinated and completed in a very narrow time frame so the fluctuations in room temperature are negligible. This difficulty can be circumvented in future work by enclosing the entire test section in a controlled environment with preset temperature and humidity controls.

To visualize the convective mechanisms present during the solidification process, a modified Shadowgraph technique was utilized. This method resulted in a much higher contrast in the visualization of the density gradients within the plume. With a conventional Shadowgraph method, the images are two-dimensional as the resultant images are integrated over the whole depth of the test section and projected to a flat screen. Also, the need to implement a parallel light source makes the setup for a Shadowgraph technique more difficult and the generally non-uniform illumination

doesn't provide for very appealing images. With the visualization method used in this study, the implementation procedure is highly simplified and high-resolution images of the plumes and other convective phenomena present in the flow field are clearly visible. This allows for better determination of the location of the plumes and chimneys during the solidification process and provides a marked improvement in image quality compared to previous visualizations.

For quantitative measurements of the convective mechanisms within the flow, a non-intrusive measurement technique called MTV was implemented. The advantage of this approach compared to other velocity measurement techniques like particle-based method is that this technique uses a molecular scale probe which produces a minimal effect on the very sensitive flow field within the bulk fluid. This technique was used to measure one and two-component velocities within the flow field. Above the mushy region where there are no plumes present, a two-component velocity measurement was implemented which yielded velocities on the order of 1mm/s. For measurements of the plume, a combination of the one-component and two-component techniques was necessary to characterize the whole plume. Measured velocities within the plume exhibited a magnitude of ~ 7mm/s which is consistent with previous measurements made by Wirtz et. al. (1998).

The velocity measurements obtained in this study and the previous one conducted by Wirtz et. al. (1998) are dissimilar with the work done by Magirl and Incropera (1993) due to the different cooling rates used in the two experiments. The initial goal of our study was to provide a database for comparison with a numerical simulation to characterize flow conditions present during the solidification process. In order to simplify

the numerical simulation in future work, the final temperature of the base plate is set to only -14°C, so that the solidus front does not form, as compared to -30°C in the measurements made by Magirl and Incropera. However, due to the lower cooling rate used in this study, the velocity measurements are inherently lower than those reported by other researchers using a lower temperature.

To better understand the porosity of the mush, the average speed of the fluid that traverses different locations were computed and showed that the speed is typically higher at a higher location within the test section. This is especially obvious at 8 and 16 minutes into the solidification process. The information provided here could then be used in future computation analysis for the calculation of porosity within the mush.

The current work uses a single plane measurement technique. Thus all velocity measurements are made in two dimensions. To account for out of plane motion and the three-dimensional nature of the plume, measurement of three components of the flow field would require stereoscopic MTV. A stereoscopic implementation of MTV is discussed in Bohl et. al. (2001).

# APPENDICES

# APPENDIX A

## Molecular Tagging Velocimetry (MTV) and Ammonium Chloride Chemical Mix Formulas

Formulas for calculating weight percentage and MTV Triplex concentration

Ammonium chloride ($NH_4Cl$) amount corresponding to a 26 Weight Percentage

For 26 Weight Percentage:

$$\frac{m_{NH_4Cl}}{m_{NH_4Cl} + m_{h_2o} + m_{MTV}} X100 = 26\%$$

$$m_{NH_4Cl} = 0.26m_{NH_4Cl} + 0.26m_{h_2o} + 0.26m_{MTV}$$

$$0.74m_{NH_4Cl} = 0.26m_{h_2o} + 0.26m_{MTV}$$

$$m_{NH_4Cl} = \frac{0.26}{0.74}(m_{h_2o} + m_{MTV})$$

The equation above can be simplified to exclude the weight of the MTV chemicals, since it is added in small amounts. Below show the calculations for different weight percentage used for the lifetime measurements.

4% Weight : $m_{NH_4Cl} = \frac{0.06}{0.94} m_{h_2o} = \frac{0.06}{0.94}(1500g) = 94.745g$

$$8\%\ \text{Weight}: m_{NH_4Cl} = \frac{0.08}{0.92} m_{h_2o} = \frac{0.08}{0.92}(1400g) = 121.739g$$

$$10\%\ \text{Weight}: m_{NH_4Cl} = \frac{0.10}{0.90} m_{h_2o} = \frac{0.10}{0.90}(1400g) = 155.556g$$

$$12\%\ \text{Weight}: m_{NH_4Cl} = \frac{0.12}{0.88} m_{h_2o} = \frac{0.12}{0.88}(1300g) = 177.273g$$

$$16\%\ \text{Weight}: m_{NH_4Cl} = \frac{0.16}{0.84} m_{h_2o} = \frac{0.16}{0.84}(1300g) = 247.619g$$

$$20\%\ \text{Weight}: m_{NH_4Cl} = \frac{0.20}{0.80} m_{h_2o} = \frac{0.20}{0.80}(1200g) = 300.000g$$

$$24\%\ \text{Weight}: m_{NH_4Cl} = \frac{0.24}{0.76} m_{h_2o} = \frac{0.24}{0.76}(1100g) = 347.368g$$

In calculating the amounts of the MTV chemicals to add, the following formulas were used:

Known concentration of the triplex chemicals for effective tagging:
Cyclodextrin Concentration: 2.0--4.0 x$10^{-4}$ M
Alchohol Concentration: 0.06 M
Bromo-naphtalene: For 1liter of volume, use less than 1ml, about an inch height of the small vial.

Formulas for calculating amount of chemicals to add to a specific volume of fluid

$$m_{CD} = Volume(liter) * Molar - Concentration * \frac{1300g}{mol}$$

$$V_{alcohol} = Volume(liter) * Molar - Concentration * \frac{100g}{mol} * \frac{1ml}{0.9624g}$$

*Bromonapthalene Concentration: Add to saturation*

# APPENDIX B

## Timing Diagram of Gate Signals to the Xybion Camera

## And Laser

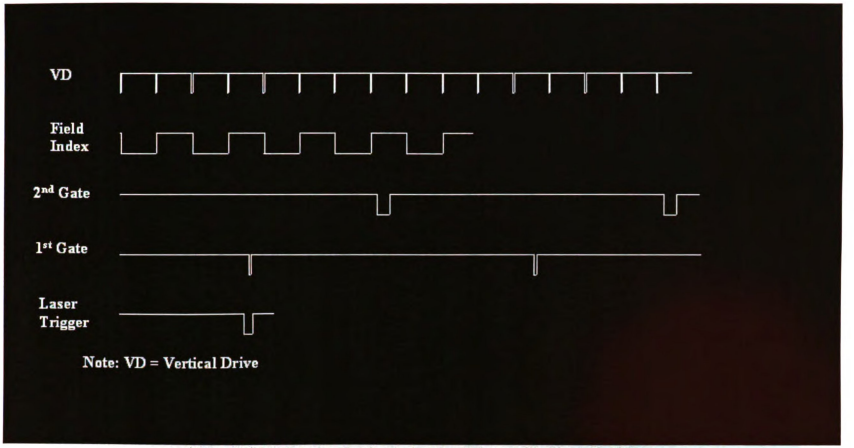


Figure B1. Timing signals of gate signals with respect to the vertical drive

The vertical drive of the camera controls the timing sequence of the gate signals. To ensure that the camera always trigger off the correct vertical drive, a field index is used to isolate one set of vertical drives. The first gate shutters the camera to obtain the undelayed image while the second gate allows the delayed image to be captured. A second delay generator is used to trigger the laser just before the first gate triggers.

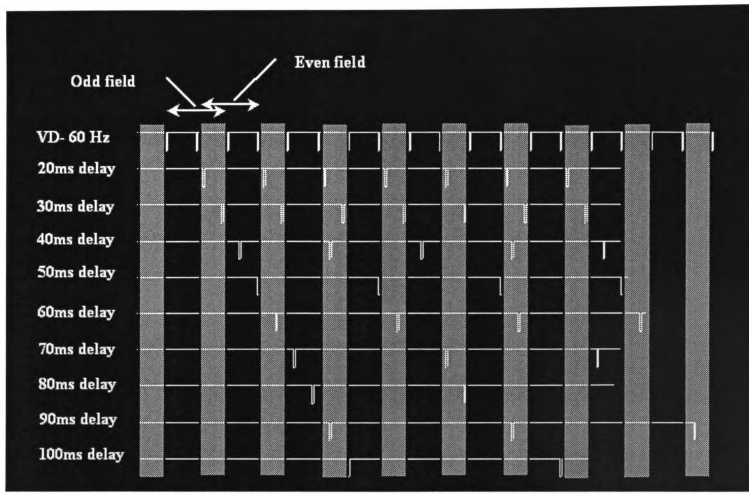


Figure B2. Timing diagram for different delay times with respect to the vertical drive

The gating signals need to fall within the shaded regions to be integrated in full frame mode. Example images at 40ms show that only one field is exposed due to the fact that the gating period did not fall within the shaded region

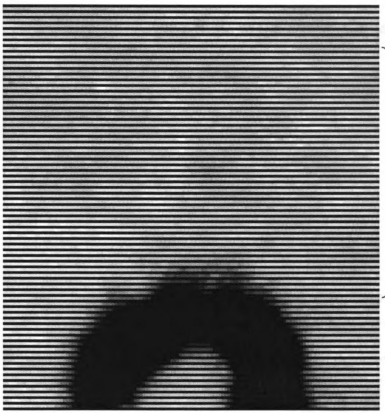


Figure B3. Sample image of gating the camera in an odd or even field

# APPENDIX C

## X-Y Ratio of the Xybion Camera

To ensure that the camera used had the same pixel dimensions in the X and Y direction, an image was taken using the Xybion camera to verify this. If the X-Y ratio is the same, the scale image for experiments using the camera only needs to be in either the X or Y direction.

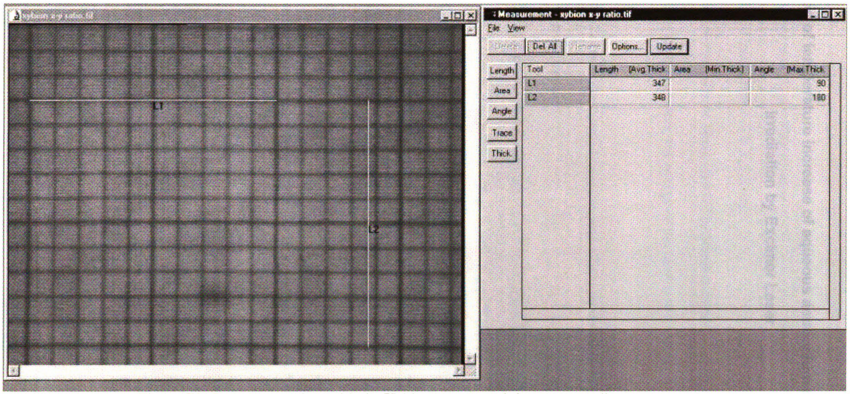


Figure C1. Scale image taken with the Xybion camera and the corresponding measurements

From the picture above, it is seen that the X-Y ratio of the CCD on the Xybion camera is similar - with a difference of one pixel that is negligible. Thus it can be assumed safely that 35pixels in the x direction is 35pixels in the y direction in actual measurement

# APPENDIX D

## Calculation of temperature increase of aqueous ammonium chloride due to irradiation by Excimer Laser

## Temperature Increase of Fluid Due to UV Laser Illumination

- Laser energy used $E_{max}$ = 100mJ/pulse
- Size of main laser beam = 3.8 X 1.3 cm
- Approximate size of laser beam after VFL: 60mm x 1mm
- Using a 50/50 beam splitter, the energy of the laser is divided into 2 beams of equal intensity
- Assuming 21 thick lines (worst case scenario where the lines are much thicker than the actual beam blockers)
- Total area where laser passes through = (21 x 0.015cm)x 1mm = $3.15 \times 10^{-6} m^2$
- Fraction of energy that passed by = $3.15 \times 10^{-6} / 60 \times 10^{-6} \sim 0.05$

Volume of fluid irradiated, V = 21 x 1mm x 0.015cm = $3.15 \times 10^{-8} m^3$

$m_{AmCl} = \rho V = 1078 \times V = 3.39 \times 10^{-5}$ kg

$Q = mC_p\Delta T = 3.39 \times 10^{-5} kg \times (3.249 kJ/kg.K) \times \Delta T = 10mJ$

$\Delta T = 0.09$ K

we have assumed that $\alpha = 1$ whereby all the laser is absorbed by the fluid.

# BIBLIOGRAPHY

## Bibliography


Beckerman, C.; Wang, C.Y., 1996, "Equiaxed dendritic solidification with convection: Part III. Comparisons with $NH_4Cl$-$H_2O$ experiments," Metallurgical and Materials Transactions A, **27A**, pp. 2784-2795.

Bohl, D.G., Koochesfahani, M.M. and Olson, B.J., 2001, "Development of stereoscopic molecular tagging velocimetry," Experiments in Fluids, **30**, pp. 302-308.

Chen, C.F. and Chen, F., 1991, "Experimental study of directional solidification of aqueous ammonium chloride solution," J. Fluid Mech., **227**, pp. 567-586.

Cohn, R.K. and Koochesfahani, M.M., "The accuracy of remapping irregularly spaced velocity data onto a regular grid and the computation of vorticity" Experiments in Fluids," Experiments in Fluids, **29**, pp. 61-69

Gendrich, C.P. and Koochesfahani, M.M., 1996, "A spatial correlation technique for estimating velocity fields using molecular tagging velocimetry (MTV)," Experiments in Fluids, **22**, pp. 67-77.

Gendrich, C.P., Koochesfahani, M.M. and Nocera, D.G., 1997, "Molecular Tagging Velocimetry and other novel applications of a new phosphorescent supramolecule," Experiments in Fluids, **23**, pp. 361-372

Hellawell, A, Sarazin, J.R. and Steube, R.S., 1993, "Channel convection in partly solidified systems," Phil. Trans. R. Soc. Lond. A, **345**, pp. 507-544.

Incropera F.P. and Magirl, C.S., 1993, "Flow and Morphological Conditions associated with Unidirectional Solidification of Aqueous Ammonium Chloride," Transactions of the ASME, **115**, pp.1036-1043.

Koochesfahani, M.M., 1999, "Molecular Tagging Velocimetry (MTV) Progress and Applications (Invited),AIAA Paper 99-3786," 30$^{th}$ AIAA Fluid Dynamics Conference, 28 June-1 July 1999.

Koochesfahani, M.M., Cohn. R.K., Gendrich, C.P. and Nocera, D.G., 1996, "Molecular tagging diagnostics for the study of kinematics and mixing in liquid phase flows", Presented at the Plenary Session of the Eight International Symposium on Applications of Laser Techniques to Fluid Mechanics, Lisbon, Portugal, July 8-11, 1-12

Liu, S. and Hellawell, A, 1999, "Experiments with constrained chimney-plume flows in the system ammonium chloride-water: comparison with unconstrained case," J. Fluid Mech., **388**, pp. 21-48.

Magirl, C.S. and Incropera, F.P., 1993, "Flow and morphological conditions associated with unidirectional solidification of aqueous ammonium chloride", J. Heat Transfer, **115**, 1036-1043.

Prescott, P.J. and Incropera, F.P., 1996, "Convective heat and mass transfer in alloy solidification," Advances in Heat Transfer, **28**, pp.231-238.

Solomon, T.H. and Hartley, R.R., 1998, "Measurements of the temperature field of mushy and liquid regions during the solidification of aqueous ammonium chloride", J. Fluid Mech., **358**, pp 87-106.

Schulze, T.P. and Worster, M.G, 1998, "A numerical investigation of steady convection in mushy layers during the directional solidification of binary alloys", J. Fluid Mech., **356**, pp.199-220.

Wang, S.Y., Liu, Y.Z., Lin, C.X. and Ebadian, M.A., 1998, "Double diffusive velocity measurement during the solidification process using particle image velocimetry" Proceedings of the ASME Heat Transfer Division, HTD-Vol 361-4, pp. 111-118.

Wang, S.Y., Lin, C.X. and Ebadian, M.A., 1999, "Study of double diffusive velocity during the solidification process using particle image velocimetry Int. J. Heat Mass Transfer, **42**, pp. 4427-4445.

Wang, S.Y., Lin, C.X. and Ebadian, M.A., 1999, "Vortex flow of low concentration $NH_4Cl$-$H_20$ solution during the solidification process" Int. J. Heat Mass Transfer, **42**, pp. 4153-4163.

Wöllhover, K., Körber, Ch., Scheiwe, M.W. and Hartmann, U., 1985, "Unidirectional freezing of binary aqueous solutions: an analysis of transient diffusion of heat and mass" Int. J. Heat Mass Transfer, **28-4**, pp. 761-769.

Worster, M.G, 1997, "Convection in mushy layers" Annu. Rev. Fluid Mech. **29**, pp. 91-122.

Wirtz, K., Koochesfahani, M., McGrath, J.J. and Benard, A., 1998, "Molecular Tagging Velocimetry applied to buoyancy-driven convective phenomena during solidification," Proceedings of the ASME Heat Transfer Division, **4**, pp. 103-110.

Wirtz, Kay, 1998, "Experimental study of convection phenomena associated with solidification processes", Diplomarbeit thesis, RWTH-Aachen, conducted at Mechanical Engineering Department, Michigan State University

## General References

Chen, Y. -J. and Davis, S.H., 1999, "Directional solidification of a binary alloy into a cellular convective flow: localized morphologies", J. Fluid Mech., **395**, pp. 253-270.

Schulze, T.P. and Worster, M.G., 1999, "Weak convection, liquid inclusions and the formation of chimneys in mushy layers", J. Fluid Mech. **388**, pp.197-215.

Liu, S. and Hellawell, A., 1999, "Experiments with contrained chimney-plume flows in the system ammonium chloride-water: comparison with the unconstrained case", **388**, pp. 21-48.

Cummings, L.M., Hohlov, Y.E., Howison, S.D. and Kornev, K, 1999, "Two-dimensional solidification and melting in potential flows", **378**, pp. 1-18.

Griffiths, R.W. and Fink, J.H., 1997, "Solidifying Bingham extrusions: a model for the growth of silicic lava domes", **347**, pp. 12-36.

Wettlaufer, J.S. and Worster, M.G., 1997, "Natural convection during solidification of an alloy from above with application to the evolution of sea ice", **344**, pp. 291-316.

Schiaffino, S. and Sonin, A.A., 1997, "Formation and stability of liquid and molten beads on a solid surface", **343**, pp. 95-110.